Distribution, microphysical properties, and tectonic control of deformation bands in the Miocene accretionary prism (Whakataki Formation) of the Hikurangi subduction zone

Kathryn E. Elphick[1], Craig R. Sloss[1], Klaus Regenauer-Lieb[2], Christoph E. Schrank[1]

5   [1]School of Earth and Atmospheric Sciences, Queensland University of Technology, GPO Box 2434, Brisbane, QLD 4001, Australia.
[2]School of Petroleum Engineering, University of New South Wales, Sydney, NSW, Australia

Correspondence to: Kathryn Elphick (elphickk@qut.edu.au)

Abstract

10   We analyse deformation bands related to both horizontal contraction and horizontal extension in Miocene turbidites of the Whakataki Formation south of Castlepoint, Wairarapa, North Island, New Zealand. In the Whakataki Formation, four sets of cataclastic deformation bands are identified: [1] normal-sense Compactional Shear Bands (CSBs); [2] normal-sense Shear-Enhanced Compaction Bands (SECBs); [3] reverse-sense CSBs; and [4] reverse-sense SECBs. During extension, CSBs form most frequently with rare SECBs. Extensional CSBs

15   are often, but not exclusively, associated with normal faults. During contraction, distributed SECBs are observed most commonly, sometimes clustering around small reverse faults and thrusts. Contractional CSBs are primarily found in the damage zones of reverse faults. The quantitative spacing analysis shows that most outcrops are characterised by mixed spatial distributions of deformation bands, interpreted as a consequence of overprint due to progressive deformation or distinct multiple generations of deformation bands from different deformation

20   phases. Since many deformation bands are parallel to adjacent juvenile normal- and reverse-faults, bands are likely precursors to faults. With progressive deformation, the linkage of distributed deformation bands across sedimentary beds occurs to form through-going faults. During this process, bands associated with the wall-, tip-, and interaction damage zones overprint earlier distributions resulting in complex spatial patterns. Regularly spaced bands are pervasively distributed when far away from faults. Microstructural analysis shows that all

25   deformation bands form by inelastic pore collapse and grain crushing with an absolute reduction in porosity relative to the host rock between 5 and 14%. Hence, deformation bands likely act as fluid flow barriers. Faults and their associated damage zones exhibit a spacing of order ten metres on the scale of 10 km and are more commonly observed in areas characterised by higher mudstone to sandstone ratios. As a result, extensive clay smear is common in these faults, enhancing the sealing capacity of faults. Therefore, the formation of deformation

30   bands and faults leads to progressive flow compartmentalisation from the scale of ten metres down to about ten centimetres, the typical spacing of distributed deformation bands.

1.   Introduction

Deformation bands are defined as tabular, oblate zones of localised plastic shear and volume change produced through inelastic yielding in granular material (porosity >5%) (Aydin, 1977, 1978; Aydin and Johnson, 1983;

35   Okubo and Schultz, 2005; Schultz and Siddharthan, 2005). Bands often exhibit mm- to cm- offset, but do not act

as planes of displacement discontinuity, distinguishing them from faults (Świerczewska and Tokarski, 1998).
Kinematic classification recognises five types of deformation band: pure compaction bands, compactive
shear bands, isochoric shear bands, dilatant shear bands, and pure dilation bands (Fossen et al., 2007; Eichhubl et
al., 2010). In nature, shear bands with associated compaction are most commonly observed, formed by grain
40   rearrangement with or without cataclasis (Fossen et al., 2007). Besides its relevance for understanding strain
localisation in rocks, the study of deformation bands is important because of their sealing potential and effect on
fluid flow in hydrocarbon and groundwater reservoirs (Antonellini and Aydin, 1994; Ogilvie and Glover, 2001;
Fossen and Bale, 2007; Fossen et al., 2007; Ballas et al., 2013; Ballas et al., 2015; Qu et al., 2017; Fossen et al.,
2018). Deformation bands commonly exhibit a reduction in permeability compared to the host rock, subsequently
45   acting as barriers to fluid flow (Ogilvie et al., 2001; Ogilvie and Glover, 2001; Fossen and Bale, 2007; Fossen et
al., 2007; Ballas et al., 2015; Fossen et al., 2018). The extent to which deformation bands can impact reservoir
fluid flow depends not only on their hydraulic properties but also their spatial distribution (Ogilvie and Glover,
2001; Sternlof et al., 2006; Fossen and Bale, 2007; Torabi et al., 2013; Ballas et al., 2015). In nature, deformation
bands exhibit two spatial distributions: [1] networks of bands concentrated into clusters or zones in the vicinity of
50   faults (Antonellini and Aydin, 1995; Shipton and Cowie, 2001, 2003; Soliva et al., 2013; Ballas et al., 2014), and
[2] a pervasive periodic and/or clustered distribution across a deformed region, unrelated to faults (Saillet and
Wibberley, 2010; Ballas et al., 2013; Soliva et al., 2013; Soliva et al., 2016). Field studies suggest that the spatial
distribution of deformation bands is largely controlled by the tectonic regime in which they form (Saillet and
Wibberley, 2010; Solum et al., 2010; Soliva et al., 2013; Ballas et al., 2014; Soliva et al., 2016). Deformation
55   bands associated with a normal faulting regime are observed in the damage zone of faults where the band density
increases as the fault plane are approached (Shipton and Cowie, 2003). Conversely, deformation bands formed
during horizontal contraction exhibit distributed, regular spacing.

Here, we analyse deformation bands formed in poly-deformed Miocene siliciclastic turbidites of the exposed
Hikurangi accretionary wedge in eastern New Zealand to test if the influence of tectonic regime documented in
60   previous studies applies. The studied rock package has been deformed in both horizontal extension and horizontal
contraction, with only minor reactivation. Previous studies on the relationship between deformation band
distribution and the tectonic environment analysed deformation bands hosted within relatively homogeneous
Aeolian sandstones in two key locations: [1] Utah, USA, where the deformation bands are associated with the
intracontinental Laramide orogeny (Aydin, 1978; Antonellini et al., 1994; Solum et al., 2010; Fossen et al., 2011)
65   and [2] Provence, France, where bands formed during the Cretaceous Pyrenean intracontinental mountain building
event and the subsequent Oligocene-Miocene rifting (Saillet and Wibberley, 2010; Ballas et al., 2013; Soliva et
al., 2013; Ballas et al., 2014; Soliva et al., 2016). Aeolian sandstones are not common reservoir rocks, yet much
of the analysis from previous studies focusses on how deformation bands alter the petrophysical properties of the
host rock. Few studies analysed deformation bands in an active accretionary prism (Karig and Lundberg, 1990;
70   Labaume et al., 1997; Maltman, 1998; Ujiie et al., 2004) compared to those focusing on the field sites in Utah and
Provence, and none have done so with the primary goal of testing how the tectonic setting influences the
kinematics and distribution of bands. Our study of deformation bands formed during horizontal extension and
horizontal contraction in the Hikurangi accretionary prism, therefore, tests the influence of tectonic regime in a
different tectonic environment. Besides, studies from the Provence have analysed rocks buried to 0.4-0.6 km
75   (Soliva et al., 2013) and in Utah, rocks were buried to 1-2 km (Fossen et al., 2011). The rock package studied here

has been buried to ≤ 3 km, placing the unit in the hydrocarbon formation window (Wells, 1989). Preliminary offshore drilling of the Miocene siliciclastic rock package has documented significant gas shows, and a study of the onshore analogue could provide useful insights into the reservoir architecture at depth (Field et al., 2006). Therefore, our work complements existing ones by considering rocks with different petrophysical properties, which are actively targeted by hydrocarbon exploration (Lee et al., 2002; New Zealand Petroleum & Minerals, 2013).

2. Background
2.1. Geologic setting

We study faults and deformation bands in the Whakataki Formation, an exhumed turbidite package of the accretionary prism of the Hikurangi subduction zone (Chanier and Ferrière, 1991; Neef, 1992a; Neef, 1992b, 1995; Chanier et al., 1999; Field, 2005; Nicol et al., 2007; Nicol et al., 2013). The Hikurangi subduction zone initiated ca. 25 Ma ago and accommodates oblique convergence between the Pacific and North Zealandian plates (Spörli, 1980; Walcott, 1984; Ballance et al., 1985; Walcott, 1987; Ballance, 1988; Chanier and Ferrière, 1991; Rait et al., 1991; Luyendyk, 1995; Chanier et al., 1999; Nicol et al., 2007; Bailleul et al., 2013; McCoy-West et al., 2013; Mortimer et al., 2017; Strogen et al., 2017).
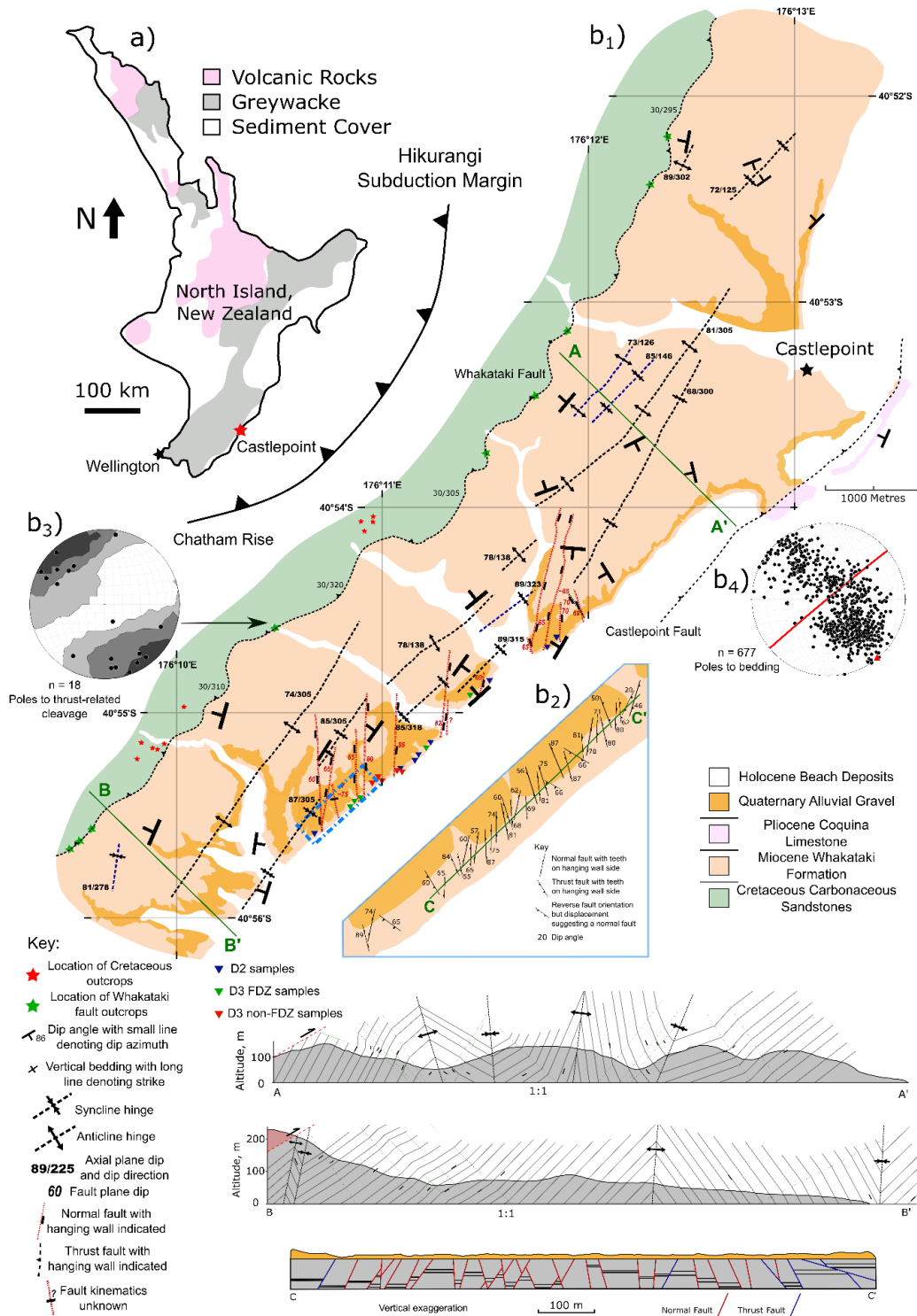
Figure 1. a) Simplified geological map (GNS, 2020) of New Zealand's North Island with study site location (red star) (coordinates: NZGD 2000, UTM Zone 60S, E: 0430670, N:5468211). **b₁)** Simplified geological map of the research area. Dominant structures in the field site are NE-SW trending folds and thrust faults with N-S trending normal faults along the coastline. Below are cross-sections through the area. A-A' and B-B' highlight the asymmetrical fold geometry with synclines resembling box-folds and anticlines resembling kink-folds. The unconformable overlying Quaternary sediments have not been plotted to highlight the geometry of the folds. C-C' is a schematic cross-section drawn perpendicular to the average strike of normal faults. An arbitrary geological bed has been added to show possibly displacements associated with faults. **b₂)** A detailed map of fault location and orientation along a ca. 1 km stretch of coastline. Normal faults are dominant, with thrust faults found in areas of low normal-fault density. **b₃)** Schmidt net with poles to cleavage planes observed in the damage zone of the Whakataki Fault, a large-scale thrust fault associated with the first phase of compression, D1. **b₄)** Schmidt net of poles to bedding planes. The mean axial plane for all bedding is plotted as great circle (red line). Given that the axial plane trends parallel to the traces of the dominant thrust faults in the area, it is reasonable to assume, by assessing the poles to the axial planes, that the folding was induced by SE shortening. All Schmidt nets are plotted with the software Stereonet 10 of Allmendinger et al. (2011).

The onset of subduction is expressed in the sedimentary record by the wide-spread deposition of olistostrome deposits in the earliest Miocene (Chanier and Ferrière, 1991; Bailleul et al., 2007; Bailleul et al., 2013), which also define the base of the studied Whakataki Formation. The basal olistostrome is overlain by deep-marine deposits to higher-energy flysch deposits (Neef, 1992a), consisting of a succession of laterally continuous fine-grained sandstone and siltstone turbidite deposits with an estimated thickness of 900-1500 m (Neef, 1992a; Field, 2005; Bailleul et al., 2013).

The present study is based on field observations and samples collected from coastal exposures of the Miocene Whakataki Formation 5 km southwest of Castlepoint, in the Wairarapa region of the North Island, New Zealand (Fig. 1, coordinates: NZGD 2000, UTM Zone 60S, E: 0430670, N:5468211). The Whakataki Formation (deposited ca. 25-17.5 Ma (Neef, 1992a; Morgans, 1997; Field, 2005; Bailleul et al., 2013)) was deposited within tectonically controlled, confined basins on the lower trench-slope of the subduction margin (Bailleul et al., 2007; Bailleul et al., 2013). The sediments preserve a record of not only the onset of subduction ca. 25-19 Ma (D1), but also a period of extension ca. 15-5 Ma (D2) and renewed contraction from the Pliocene to recent (D3) (Chanier and Ferrière, 1991; Chanier et al., 1999; Bailleul et al., 2007; Bailleul et al., 2013). Each deformation phase induced corresponding deformation structures in the field area (Fig. 1, Fig. 2):

D1: margin-perpendicular contraction expressed by both landward and seaward emplacement of thrust-sheets, gentle folding, and reverse faulting along the Hikurangi margin, with the development of trench-slope basins bound by structural highs (Bailleul et al., 2013; Chanier and Ferrière, 1991; Chanier et al., 1999; Maison et al., 2018; Rait et al., 1991). The main D1 structure in the field area is the NE-SW trending Whakataki thrust fault that has emplaced the pre-Miocene Whangai Formation onto the Miocene Whakataki Formation and acts as the western boundary to the Whakataki Formation in the field site (Fig. 2).

D2: An overall deepening of the forearc domain (Crundwell, 1987; Wells, 1989) and widespread subsidence involved margin-parallel and margin-perpendicular extension of the accretionary wedge accommodated by normal faulting (Bailleul et al., 2013; Bailleul et al., 2007; Chanier et al., 1999). Tectonic erosion, with associated syn-sedimentary gravitational collapse, has been attributed to this reversal in stress regime (Chanier et al., 1999; Bailleul et al., 2013).

D3: A renewal of dominant margin-perpendicular contraction of the wedge with associated folding, thrusting, and strike-slip faulting (Chanier et al., 1999; Nicol et al., 2002; Bailleul et al., 2007; Nicol et al., 2007; Bailleul et al., 2013). Also associated with this deformation phase is the uplift and exposure of the Coastal Ranges (Nicol et al., 2002). In the field site, this deformation phase is expressed by pervasive deformation bands, small thrust faults, and intense folding.

10.5194/se-2020-80
2020-05-18
Author(s) 2020. CC BY 4.0 License.
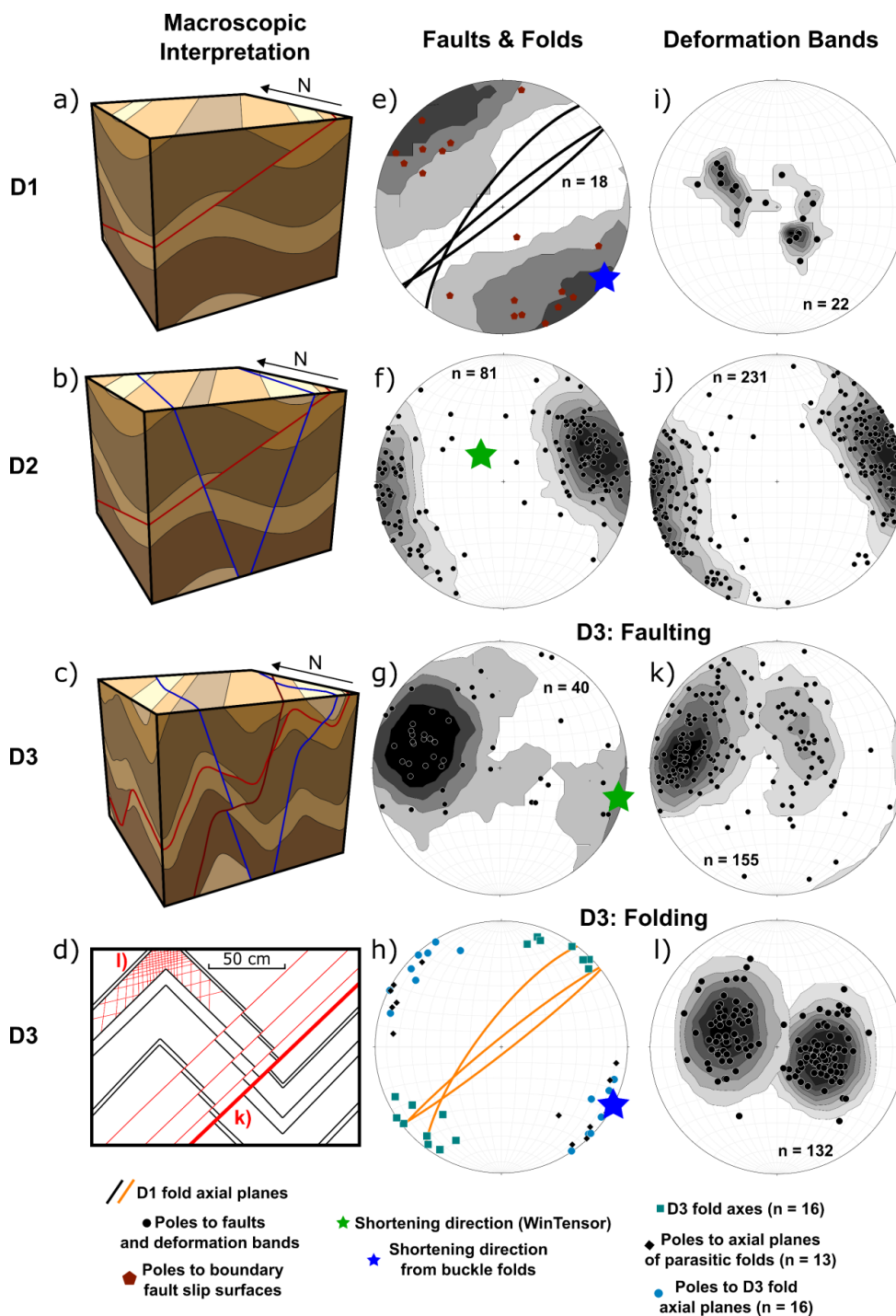
Figure 2. Tectonic evolution of the mapping area with each tectonic regime, with corresponding structural data for each phase. a), b), c): schematic block diagrams of each deformation phase. d) sketch of deformation associated with D3. During D3, two clear distributions of deformation bands are observed: deformation bands associated with faults and deformation bands observed far from faults. e) Schmidt net of D1 parasitic fold orientations (planes) with poles to slip surfaces observed in the damage zone of the large-scale Whakataki thrust fault. f), g): Schmidt nets of fault orientation data from D2 and D3 deformation, respectively. σ_1 is indicated by the green star. h) The orientation of D3 folds with D1 fold axial planes plotted to highlight the similar orientations across both events. The blue star represents the shortening direction, estimated from the pole to the average fold axial plane. i) Poles to D1 deformation bands. j) Poles to D2 deformation bands. k) Poles to D3 fault-damage-zone-associated deformation bands. l) Poles to D3 deformation bands that are not located in fault damage-zones. The similarity of the fault and fault-associated deformation band orientations indicates that they formed in the same stress field. Also, axial plane data from D3 aligns with D3 non-fault damage-zone associated bands as shown in (l). All deformation band and fault data are back tilted as there is evidence of folding occurring coeval to, or later than all events. Stereoplots were produced using Stereonet 10 software (Allmendinger et al., 2011). Paleostress analysis completed using WinTensor (Delvaux and Sperner, 2003).

2.2. Classification and microstructures of deformation bands

Deformation bands are the most common strain localisation structure observed in deformed porous rocks (Fossen et al., 2007). The bands typically have widths in the range of micrometres to centimetres and lengths most commonly > 100 m (Aydin, 1977; Antonellini et al., 1994; Aydin et al., 2006; Fossen et al., 2007). Associated displacement, if any, is often on the order of mm – cm. The displacement associated with deformation bands is less than that associated with faults/slip surfaces, permitting a distinction between the two. Deformation bands can be broadly classified in two ways; [1] by deformation mechanism and [2] by kinematics (Fossen et al., 2007).

[1] The dominant deformation mechanisms observed in deformation bands are [a] granular flow; [b] cataclasis; [c] phyllosilicate smearing; and [d] dissolution and cementation (see Fossen et al. 2007 for review). The deformation mechanism depends on the grain size, sorting, mineralogy, diagenetic history, porosity and stress state (Fossen et al., 2007) and controls petrophysical properties (Fossen and Bale, 2007; Ballas et al., 2015; Fossen et al., 2018). Disaggregation bands are associated with minor grain fracture, resulting in bands with porosities and permeabilities comparable to the host rock. However, bands formed dominantly by cataclastic deformation exhibit considerably lower porosities and permeabilities compared to the host rock. Dependent upon the host rock mineralogy, porosity can be reduced by one to two orders of magnitude, and permeability can be reduced by up to six orders of magnitude with phyllosilicate-bearing sandstones generally characterised by larger reductions (Fossen et al., 2007). Field and laboratory observations show that deformation bands are most commonly characterised by a reduction in both porosity and permeability compared to the host rock (Aydin, 1978; Aydin and Johnson, 1978; Underhill and Woodcock, 1987; Antonellini et al., 1994; Antonellini and Aydin, 1995; Fossen and Bale, 2007; Fossen et al., 2007; Torabi et al., 2013; Ballas et al., 2015; Fossen et al., 2018).

[2] Kinematically, deformation bands can be classified as compaction, dilation, shear, and hybrid bands, combining shear with compaction or dilation (Aydin et al., 2006; Fossen et al., 2007). The most common type in nature is Compactional Shear Bands (CSBs) (Fossen et al., 2007). Here, we use the kinematics-based classification system because it is most readily applied in the field. Deformation mechanisms are best assessed with microscopic methods, also done in this paper. Microstructural characteristics of deformation bands are intimately related to their kinematics and are summarised in Table 1.

180 **Table 1 Criteria to kinematically classify deformation bands (Fossen et al., 2007; Schultz, 2019).**

Physical Parameters	Effects of Deformation Bands in Host Rock						
				Compactional shear bands		Compaction bands	
	Dilation bands	Dilational shear bands	Shear bands	*Cataclastic*	*Non-cataclastic*	*Shear enhanced compaction bands*	*Pure compaction bands*
Porosity	Increase	Increase	No change	Decrease	Decrease	Decrease	Decrease
Permeability	Increase	Increase	No change	Decrease	Decrease	Decrease	Decrease
Grainsize	No change	No change (predicted)	No change	Decrease	Decrease	Decrease	Decrease
Additional comments	N/A	N/A	N/A	Considerable reduction in grainsize	Minor grain-cracking	Approx. equal amounts of shear and compaction	No detectable shear and dissolution at grain contacts

2.3. Spatial distribution of deformation bands: controls of tectonic stress regime?

Field studies demonstrate that deformation bands exhibit two spatial distributions; [1] networks of bands concentrated into clusters or zones in the vicinity of faults (Antonellini and Aydin, 1995; Shipton and Cowie,

185 2001, 2003; Solum et al., 2010; Soliva et al., 2013; Ballas et al., 2014) and [2] a pervasive periodic and/or clustered distribution across a deformed region, unrelated to faults (Saillet and Wibberley, 2010; Solum et al., 2010; Ballas et al., 2013; Soliva et al., 2013; Soliva et al., 2016). The distribution and type of deformation band that form have been linked to the tectonic stress regime (Saillet and Wibberley, 2010; Soliva et al., 2013; Ballas et al., 2014; Ballas et al., 2015; Soliva et al., 2016). In a thrust regime, periodically spaced bands with a compaction component

190 ± shear were observed. In horizontal extension, clusters of bands in fault damage zones characterised by a decay of density away from the fault plane and a large shear component ± dilation/compaction (volumetric sign dependent upon the effective mean stress) are observed. The Whakataki Formation contains deformation bands associated with horizontal extension and horizontal contraction. By analysing the distribution of deformation bands associated with each regime at Castlepoint, we test if the tectonic stress regime controls the spatial

195 distribution of the observed bands.

2.4. A conceptual mechanical model for deformation bands

The kinematics and orientation of deformation bands are commonly explained through rate-independent plasticity theory. The broadly accepted approach is called the cam-cap model of yielding and band formation (Fig. 3) (Wong et al., 1992; Schultz and Siddharthan, 2005; Fossen et al., 2007). The cam-cap yield surface often matches the

200 failure response of brittle granular media (e.g., Wong and Zhu, 1999). Triaxial deformation experiments on porous media show that their yield is a non-linear surface in Q-P-space, with a positive slope at low mean stresses and a negative slope at higher mean stresses (Fig. 3) (Wong and Zhu, 1999; Rudnicki, 2004; Karner et al., 2005). Q and P signify differential stress and effective mean stress, respectively:

$$Q = \sigma_1 - \sigma_3 \tag{1}$$

205 $$P = \left(\frac{(\sigma_1 + \sigma_2 + \sigma_3)}{3}\right) - P_f \tag{2}$$

where σ_1, σ_2 and σ_3 denote the principal stresses of the Cauchy stress tensor, and P_f is pore-fluid pressure. Kinematically, the cam-cap yield surface can explain the continuous transition from pure dilation bands to pure compaction bands, via shear bands, with its change in slope (Fig. 3) (Bésuelle, 2001). The Q-P diagram links the state of stress at the point of inelastic yielding to the kinematic type of deformation band that will form and,

210 broadly, the orientation of that band in relation to σ_1 (Fig. 3) (Fossen et al., 2007; Schultz, 2019). Dilation and compaction band orientation can be adequately predicted in Q-P space. However, the orientation of bands with

associated shear is less adequately predicted because the Coulomb criterion, used for predicting orientation, does not consider volumetric changes across a shearing surface (Schultz, 2019). If the orientation and band kinematics are known, the intersection of the yield envelope can be predicted. Current literature hypothesises that the point

215 of intersection is controlled by the tectonic regime, and therefore, the orientation and band kinematics are controlled by the tectonic regime (Soliva et al., 2013; Ballas et al., 2014; Soliva et al., 2016; Fossen et al., 2018).
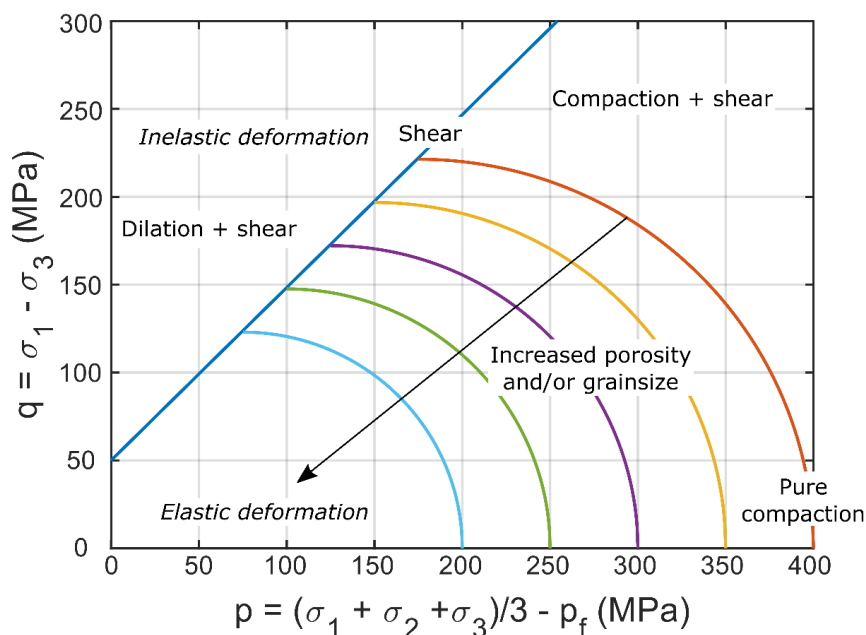
Figure 3. Cam-cap yield envelope showing the relationship between the stress state at the point of inelastic yielding and the type and orientation of the deformation band that nucleates. The yield envelope shrinks with increased porosity
220 **and/or grain size of the material.**

3. Methods

3.1. Field Data

Field mapping took place in a 17 km^2 area south of Castlepoint (coordinates: NZGD 2000, UTM Zone 60S, E: 0430670, N:5468211), in the Wairarapa region of the North Island, New Zealand (Fig. 1). While significant
225 hinterland mapping took place, coastal outcrops were the focus of the fieldwork because exposure is poor in the hinterland. A detailed sedimentological and facies analysis was conducted on sediments of the uplifted Hikurangi accretionary prism to contextualise the structural data. It will not be included in this paper and will be presented elsewhere. Orientations of structural elements including bedding planes (S_0), faults, and deformation bands were taken across the area and plotted in lower-hemisphere, equal-area stereograms (Allmendinger et al., 2011). All
230 data are shown with bedding restored to horizontal. The restoration was completed by rotating back from the associated S_0 measurement of the bed hosting the structures using Stereonet 10 (Allmendinger et al., 2011). Individual S_0 measurements were used rather than fold axes because the folds are non-cylindrical and plunge gently. All data are restored as there is evidence of rotation in almost all features (Fig. 5). Paleostress analysis of back-rotated faults was completed using Win-Tensor (Delvaux and Sperner, 2003). For this analysis, only faults

235   with unambiguous slip vectors and shear sense were used. The PBT-kinematic-axes method was used to find the
       orientation of the principal stresses. An assessment of whether faults and deformation bands form a conjugate
       (bimodal) or polymodal pattern was conducted using a statistical test developed by Healy and Jupp (2018). The
       test analyses the orientation distribution of the poles to fault planes to distinguish between bimodal and
       quadrimodal patterns. Differentiation between bimodal and polymodal is established by first finding the ratio

240   between the eigenvalues of the second-rank orientation tensor of the datasets and secondly by calculating the *p-
       value*. *P* values close to 0 describe a polymodal pattern with higher values reflecting bimodal patterns. The
       dihedral angle, the angle bisected by σ_1 (Chemenda et al., 2012), between conjugate sets of deformation bands
       was estimated from a cylindrical best fit to orientation data. The ratio of net shear/compaction ($D_s(net)/D_c$) was
       calculated using the methods from Soliva et al. (2013) and Ballas et al. (2014). These values are used to define

245   the kinematics of the deformation bands. However, these authors assumed that they cut their samples in the plane
       spanned by the smallest and largest principal strains, the orientation of which they determined from the rather
       tightly bimodal orientation patterns of the studied bands. In our case, this approach is more difficult because the
       orientation distributions are less focussed (Fig. 2). Therefore, typical geometric section errors in terms of true
       bandwidth and true shear displacement can be expected.

250   **3.2.   Spacing Analysis**

       The spacing analysis was conducted on two scales in the mapping area: [1] on macroscopic faults with > 20 cm
       offset exposed along a 5 km stretch of coastline, and [2] on deformation bands at individual outcrops exposed in
       sandstone units. For macroscopic fault spacing, the location, dip and dip direction, heave and throw, where
       possible, and shear-sense were recorded, and faults plotted onto a map. The spacing of macrofaults was measured

255   along scan-lines oriented perpendicular to the average fault strike using the ruler tool in ImageJ (Schindelin et al.,
       2012). The scan-lines were 200 m in length in an E-W orientation (orientation perpendicular to the average fault
       orientation) and had a 50 m N-S spacing. Due to the oblique relationship between the coastline and the fault strike,
       scan-lines were shifted N after 400 m, with the first scan-line located in the SW of the coastline. Twenty scan-
       lines were used to measure the spacing, and the median is reported. The use of multiple scan-lines minimises, but

260   does not eradicate, measurement errors arising from variation in fault strike and an average strike being used to
       generate the scan-line orientation. Spacing greater than 20 m was removed from the data as these points represent
       artefacts of exposure conditions. Horizontally measured spacing was corrected for the average dip of the faults
       using the sine transformation (Eq. 3).

       True spacing = spacing × sin (average dip angle)   (3)

265   The correction procedure also introduces errors because the faults do not all dip the same way. Moreover, they
       were not rotated to their original position and orientation in space. However, these are common shortcomings of
       studying fracture spacing in 2D (Soliva and Benedicto, 2005; Laubach et al., 2018). Here, we are mainly interested
       in the general shape of the spacing distribution and the order of magnitude of absolute spacing. Pearson correlation
       coefficient values were calculated for the correlation between the corrected spacing and the associated cumulative

270   distance from the start of the first scan-line. For spacing analysis of deformation bands, outcrops had to meet the
       following conditions: [1] the outcrop surface was fairly planar, and [2] the deformation bands were striking
       roughly perpendicular to the outcrop surface. Along the coastal outcrop, twelve locations showing deformation
       bands within damage zones (fault-damage-zone (FDZ) bands) and twenty-eight locations with bands showing

seemingly regular spacing, not adjacent to faults (non-FDZ bands), were selected. Photographs were taken perpendicular to the outcrop surface. Intersections of the bands with the flat outcrop surface were mapped on a suitable photographic mosaic of the outcrop. For outcrops showing conjugate sets of non-FDZ deformation bands, field overprinting criteria were used to identify the older set, which was analysed (Fig. 5). The older set was chosen as these bands formed in rock with properties closer to the undeformed state. Changes in rock properties that occur during deformation band initiation are more likely to influence the spatial position of a later set (Nicol et al., 2013; Regenauer-Lieb et al., 2013a).

For spacing measurements of deformation bands in damage zones, the fault was put into the origin of the digitised image. For non-FDZ bands, with apparent 'regular' spacing, the first band was treated as the origin of the image. Deformation band clusters were treated as single bands (Main et al., 2000). The resulting maps were exported as a binary image. Matlab (Mathworks, 2011) was used to obtain spacing statistics along scan-lines at a spacing of 1% of the image height. When the horizontal image dimension was not perpendicular to the traces of the deformation bands in the map, spacing was again corrected with the sine transformation (Eq. 3). When normalised spacing is reported for damage zones, normalisation was done by division through damage-zone width.

In addition to the analysis of natural deformation band distributions, synthetic images were created to show ideal spacing distributions and to highlight how natural variation in heterogeneous rocks and data collection error can impact the measured spacing of natural samples. Six synthetic images were produced:

[1] Deformation bands with constant spacing;

[2] Deformation bands with constant spacing and added noise to replicate measuring bias and outcrop conditions. The noise in image [2] was generated by adding an array of random values, between 0 and 0.8 of the constant spacing value, to the space. The random values are collectively characterised by a normal distribution and a median value of 0;

[3] Deformation bands spatially characterised by an exponential spatial decay away from a fault;

[4] Deformation bands characterised by an exponential spatial decay away from a fault with integrated noise. Noise in the image [4] is generated by adding values up to 0.4 of the maxima spacing onto each spacing measurement, with added values collectively characterised by a normal distribution with a median value of 0;

[5] Deformation band spacing that reflects the overprint of an equally spaced distribution [1] by an exponentially decaying damage zone [3]; and

[6] Deformation band spacing reflecting the overprint of an equal distribution with integrated noise [2] by an exponentially decaying damage zone also containing integrated noise [4].

3.3.   Microstructural Analysis

Twenty polished thin-sections from samples of host rock and deformation band were examined by back-scattered electron (BSE) imaging using a VP Zeiss Sigma scanning-electron microscope (SEM). A 10 nm carbon-coat was applied to the samples. The instrument was run using a working distance of 8 mm, an acceleration voltage of 15 kV, an aperture size of 30 µm with an angle-selected backscattered detector. Images of host rock were taken at 400 x magnification and those of deformation bands at 800 x. Multiple images were taken with a 5-10% overlap and stitched together to produce ca. 1 mm^2 image. Of the 20 samples, 5 were taken from zones showing a 'regular' spacing of D3 deformation bands with zero to minimal apparent offset. The remaining 15 samples are from fault

damage zones, 10 from D2 damage zones, and 5 from D3 damage zones (Fig. 1). For each sample, the host rock and deformation band were analysed in the same thin section. Samples were selected from different locations

315 along the coastline in attempts to analyse a broad range of lithologies. Sample locations of bands with a 'regular' spacing are more clustered as these were the most appropriate outcrops with good exposure of the facies hosting non-FDZ bands.

BSE maps were analysed for porosity and mineralogy of the samples. Grey-level slicing was used to extract four different phases from the images [1] porosity, [2] quartz, [3] feldspar, and [4] 'other' which includes reflective

320 oxide components, micas, and clays. For porosity phase analysis, the images were eroded and dilated to generate upper and lower bounds for the estimate (Fig. 4) (Liu and Regenauer-Lieb, 2011). Grain size estimates were obtained through manual tracing of grains from SEM images in ImageJ (Schindelin et al., 2012). An average of 100 intact grains were traced for the host rock and the deformation band of each sample, and the equivalent circle diameter was calculated for each polygon. Microfracture density was measured on BSE maps along 1-mm long

325 scan-lines oriented normal to the deformation bands, as in Ballas et al. (2013). Along each scan-line, intercepted microfractures were counted to produce a fracture/mm count. Twenty scan-lines were drawn with a spacing of 0.1 mm in images, and the results were averaged for deformation bands and for host rock.
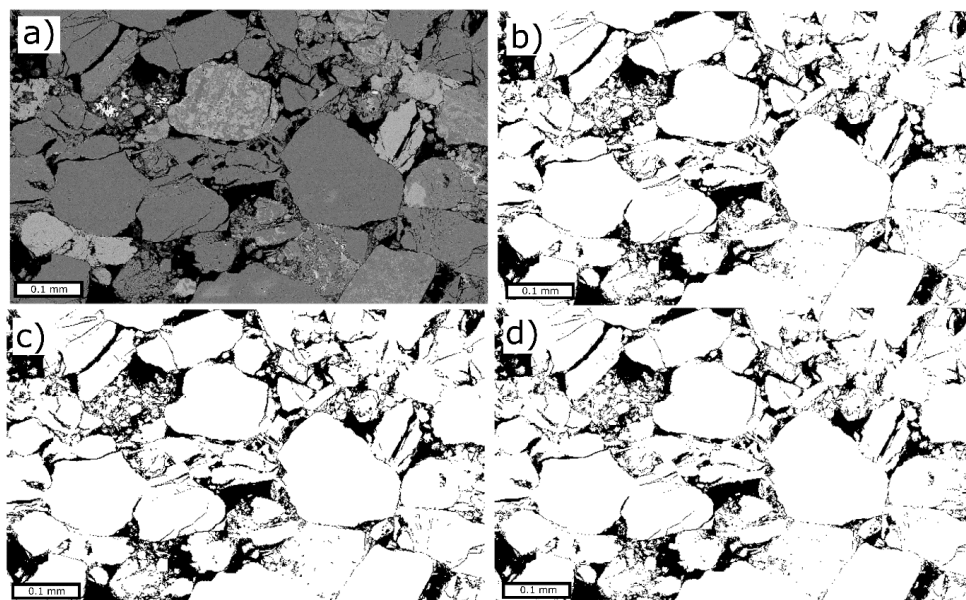
330 **Figure 4. a) Original SEM image of the host rock. b) A binary version of the original image. Calculated porosity: 17.04%. c) Eroded image. Calculated porosity: 18.22%. d) Dilated image. Calculated porosity: 15.84%. Erosion and dilation are completed to produce upper and lower bounds of which error bars can be established in the porosity estimates as shown in Figure 9.**

4.   Results

4.1.   Rock Descriptions and Structure

All three regional deformation phases discussed above (Setting 2.1) can be recognised in the Whakataki Formation. Expressions of the deformation in the Whakataki Formation include folds, faults, and deformation bands. Deformation bands are most common within sandstone units in areas characterised by equal sandstone to mudstone ratios, or areas where sandstone beds are dominant. In areas dominated by mudstone, bands are less common.

In the following, we describe structures associated with each tectonic phase. Throughout this description, we use Anderson's nomenclature (Anderson, 1951) where the normal-faulting regime reflects a (sub-)vertical σ_1 (horizontal extension) and a thrust-faulting regime reflects a (sub-)horizontal σ_1 (horizontal contraction). A summary of the results is shown in Table 2.

Table 2 Primary results from the analysis conducted at Castlepoint.

		Normal Fault Regime (D2)	Thrust Fault Regime (D3)	
Macroscopic	Macroscopic structures	Normal faults	Reverse faults	Folds
	Fault pattern	Polymodal	Polymodal	Bimodal
	Mean vector	Not applicable	Not applicable	87/310 (axial plane)
	Corrected fault spacing (median)	8.7 m	9.3 m	Not applicable
Mesoscopic	Deformation band kinematics	Normal-sense	Reverse-sense	No observable offset/reverse-sense
	Deformation band type	Compactional shear band	Compactional shear band	Shear enhanced compaction bands and Compactional shear bands
	Location	Proximal to faults	Proximal to faults	Not associated with faults
	Dominant deformation band distribution	Aperiodic	Aperiodic	Periodic
	Fault pattern	Polymodal	Polymodal	Bimodal
	Mean vector	Not applicable	Not applicable	32/110 & 30/280
Microscopic	Absolute porosity reduction	7.90%	7.70%	9.70%
	Grainsize reduction	35%	63%	44%
	Cataclastic matrix	Present	Present	Present
	Band borders	Diffuse	Diffuse	Diffuse
	Microscale width	1.23 mm	1.53 mm	0.70 mm
	Host rock microfracture density	8.5 fractures/mm^2	6.3 fractures/mm^2	6.3 fractures/mm^2

4.2.   D1 Horizontal Contraction

4.2.1.   Faults and Folds

The main regional fault associated with D1 horizontal contraction is the lower Miocene NE-SW trending Whakataki thrust fault (Fig. 1) (Bailleul et al., 2013; Maison et al., 2018). Rare exposures of the thrust damage zone contain slip planes which indicate a shallow NW dip (30°). NE-trending km-scale folds in the hinterland define the topography (Fig. 1). Structures associated with D3 horizontal contraction have similar orientations to D1 structures (Fig. 2). With poor hinterland exposure, it is not possible to determine when the large-scale folds nucleated. Rare metre-scale, NE-trending upright, moderately NE-SW-plunging, open D1 folds are still preserved in the area (Fig. 2).
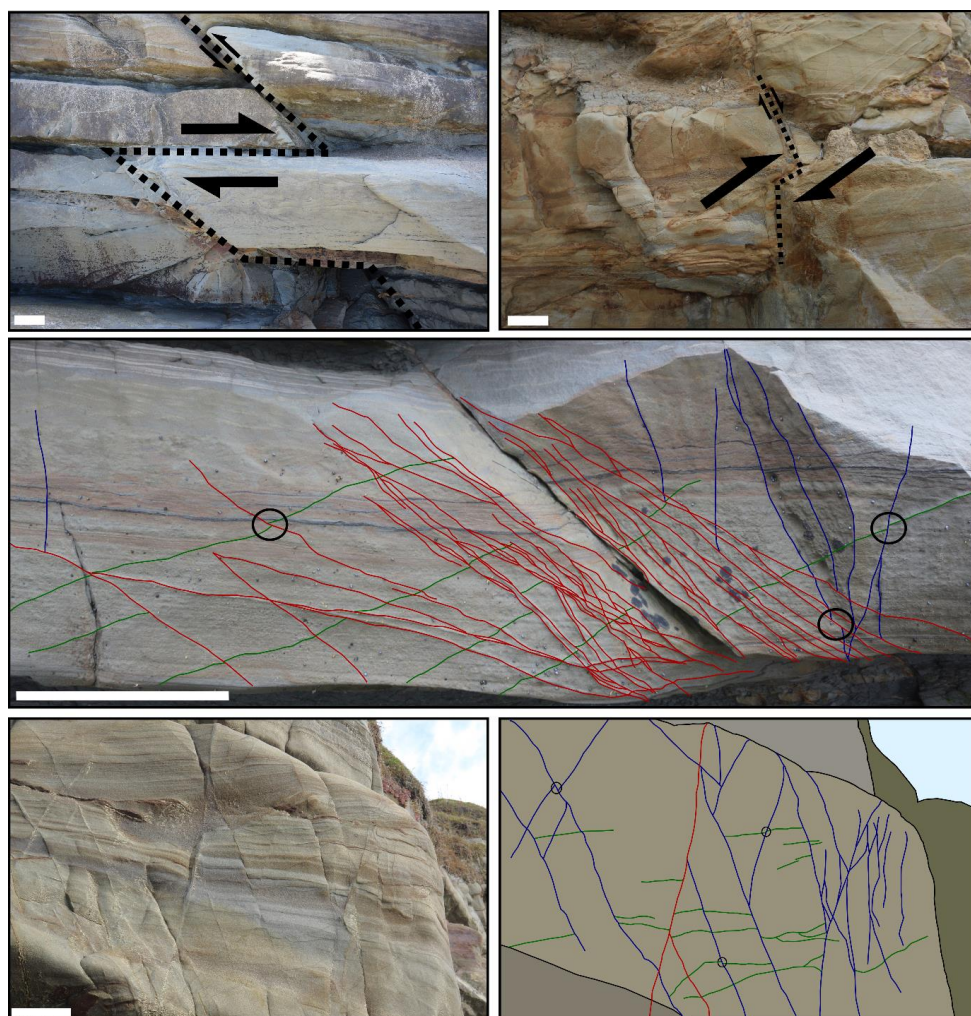
Figure 5. Examples of overprinting criteria used to determine the relative timing of each deformation phase. a) layer-parallel slip offsetting a D3 reverse fault; b) D3 reverse fault offsetting D2 normal fault; c) multiple generations of deformation band located within a D3 damage zone (green = D1, blue = D2, red = D3); d and e) multiple generations of deformation band with overprints. The scale bar in all images is 20 cm.

4.2.2.   Deformation Bands

D1 deformation bands are rare and are distinguished from D2 and D3 deformation bands through cross-cutting relationships (Fig. 5). The orientation distribution of D1 deformation bands can be considered bimodal with a *p-value* of 0.5. D1 dihedral angle ranges from 65° to 84° with a mean of 73°. With bedding restored to horizontal, deformation bands trend 037°. The set dipping SE has a dip angle of 40° and the set dipping NW dips at 26°. When bands pass through beds with thin clay-rich layers, they have a dark colour without relief. In beds with lower clay content, bands show high to moderate relief and are lighter in colour (Fig. 5). The width of bands ranges from 0.2 to 0.5 mm. Bands can extend for metres along strike. Eye and ramp structures are present, however, single strands are most commonly observed (Antonellini and Aydin, 1995). Offset associated with the bands is variable, with some characterised by minimal offset, yet others accommodate reverse shear offsets at the

millimetre scale. Conclusively, this data suggests that CSBs and Shear-Enhanced Compaction Bands (SECBs) formed during D1 horizontal contraction (Ballas et al., 2014; Fossen et al., 2018; Schultz, 2019). The rarity of D1 deformation bands does not permit for meaningful spacing analysis.

4.3.   D2 Horizontal Extension

4.3.1.   Structures and Relative Timing

Field overprinting criteria demonstrate that an extensional event followed D1 horizontal contraction (Fig. 5) (Chanier et al., 1999). Overprinting relations include the displacement of D1 fold hinges by D2 normal faults and normal-sense shear displacement of D1 deformation bands by D2 deformation bands. The structures associated with D2 are [1] normal faults; [2] deformation bands with clear normal-sense offset and [3] deformation bands with minimal offset.

4.3.2.   Faults

Normal faults are the main structures associated with D2 (Fig. 6). They trend NNW with an average dip angle of 69° (Fig. 2). Analysis of the fault pattern shows that it is polymodal with a *p-value* of 0.001 (Healy and Jupp, 2018). Fault displacement ranges from centimetres to tens of metres. Many D2 faults have displacements of ca. 1 m. The limited vertical extent of the cliff exposures and poor hinterland exposure preclude estimates of upper-bound displacement. Fault length can also not be determined as they generally extend beyond cliff height. The faults are dominantly brittle, with gouge present in the core of larger faults.
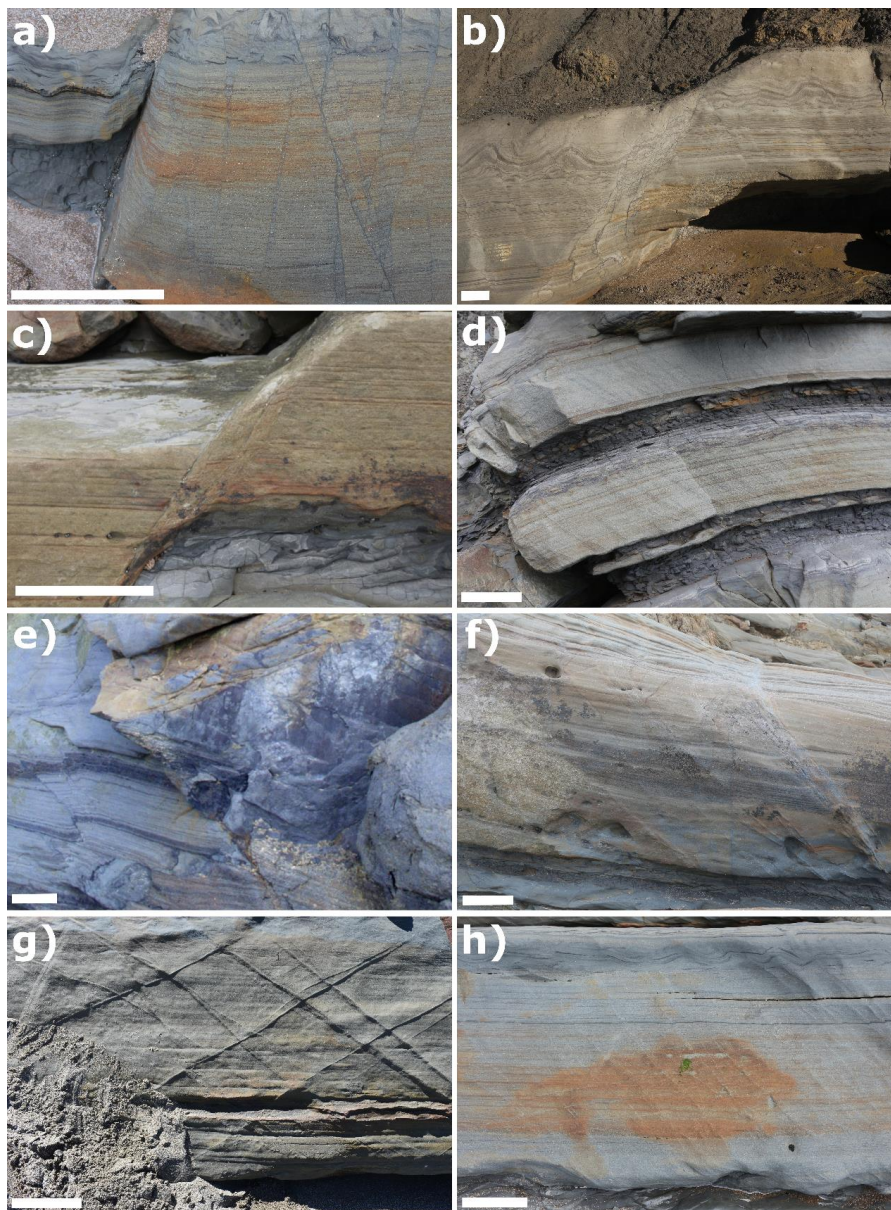
390

Figure 6. Outcrop-scale images of faults and deformation bands with a 20 cm scale bar in all images. (a), (b), & (c) show D2 normal faults with associated deformation bands. Deformation bands are darker in colour than the host rock and show minimal relief, sometimes making them difficult to observe. (d) and (e) show small D3 thrust faults and associated deformation bands. (f) shows a cluster of reverse sense deformation bands with associated offset ca. 2 cm.
395   **In the footwall of the cluster there are single reverse-sense deformation bands with similar orientation to the clusters, representing a damage zone of the cluster. D3 bands are generally lighter in colour compared to the host rock and show a higher relief than D2 bands. However, as shown in (e) D3 bands can accommodate clay smear when associated with a fault and strongly resemble D2 bands. D3 bands can be observed in clusters (d) or as single bands (e) and (f). (g), & (h) show D3 deformation bands not associated with faults. Two sets of bands are observed in (g). (h) has a dominant**
400   **set of 'regularly' spaced bands (top left of the image to the bottom right) with 2/3 bands of an opposing dip. Due to the dominant compaction kinematics, the relative timing of sets can be difficult to distinguish as they may not offset one another.**

Paleostress analysis of 16 back tilted normal faults indicates ENE-WSW extension (σ_1: 62/298°) (Fig. 2), consistent with the more comprehensive D2 paleostress analysis presented by Chanier et al. (1999) for the North Island east coast.

4.3.3.   Deformation Bands

D2 deformation bands are primarily observed in the damage zones of D2 faults. However, some single bands are observed between faults (Fig. 6). They are generally darker in colour compared to the host rock and show no or negative relief (Fig. 6). When suitable host-rock layers are present, clay smear is common (Fig. 6). When propagating through layers rich in shell hash, the bands show positive relief. The average trend of bands is 340°, with two sets of poles spanning finite arcs dipping steeply NE and SW (Fig. 2) (average dip angle is 75°). Band orientation ranges from ca. 40-60° to σ_1 indicative of CSBs and SECBs. The bands most commonly occur as single bands; however, clusters restricted to sandstone beds are also observed. Clusters localise into single strands if they propagate into adjacent mudstone beds. Band thickness ranges from 0.1 cm to 0.35 cm, with an average thickness of 0.16 cm. No obvious variation in thickness is observed in the bands along their length, which typically is on the order of tens of metres. Many D2 bands extend beyond the outcrop scale, making accurate estimates of length impossible. Bands hosted in areas dominated by sandstone, with only very thin mudstone intervals, extend beyond the outcrop scale through the mudstone. In areas characterised by thicker mudstone intervals, bands are restricted to sandstone intervals. Displacement associated with the bands generally ranges from 0 cm to 4 cm with the mean displacement ca. 1 cm. Bands without apparent offset are rare and may be an artefact of a sectioning effect (Soliva et al., 2013). Pattern analysis of the band orientation distribution shows that bimodality can be rejected with a *p-value* of 0.01 (Healy and Jupp, 2018). The dihedral angle cannot be found. Therefore, the bands must be classified through microstructural analysis and characterisation. However, in many cases, band-parallel displacement is much larger than band width. So, the shear component is likely dominant kinematically indicating that most bands are CSBs, as confirmed microstructurally below.
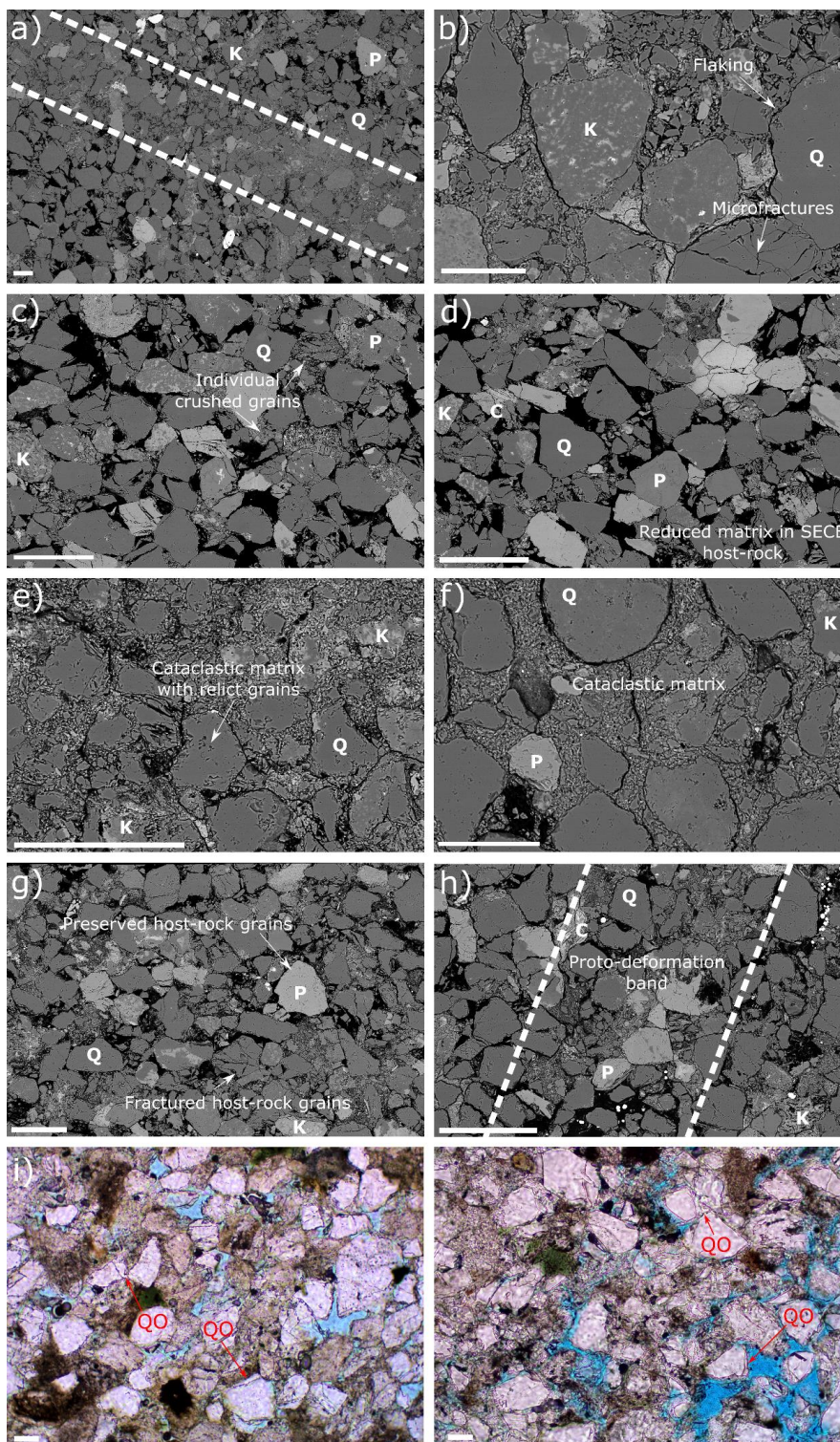
Figure 7. (a) – (h) SEM images of deformation bands and host rock – scale bar in all images is 100 µm. (a) overview image of a D3 SECB within the host rock. Diffuse edges to the band can be observed. (b) D3 SECB showing radiating fractures from grain contacts and larger grains within a fine-grained cataclastic matrix. (c) and (d) host rock surrounding D3 SECBs. Areas of crushed grains can be observed. Generally, the grains show minor fracturing and are well preserved with clear pore space between grains. (e) D3 reverse-sense CSB showing cataclastic matrix, fractured grains and minimal pore space. (f) D2 normal-sense CSB with less deformed grains preserving a larger grain size within a cataclastic matrix containing flakes and fine-grained, fractured material from the surrounding grains. (g) host rock surrounding D2 normal-sense CSBs with pockets of cataclasis from crushed grains but general preservation of grain size and porosity. (h) host rock surrounding D2 normal-sense CSB showing the alignment of pockets of cataclasis from the crushing of grains and filling in of pore space representing a nascent deformation band. (i) and (j) Light microscopy images of the host rock. In the image, quartz overgrowths (QO) are highlighted. P = Potassium Feldspar, Q = Quartz, F = Plagioclase Feldspar.

At the microscale, D2 bands are characterised by a reduction in grain size and porosity compared to the host rock which makes the bands easy to identify under the microscope (Fig. 7, Fig. 9). The bands show diffuse borders with the surrounding host rock. The grain size distribution of deformation bands generally shows positively skewed distributions with a lower median value compared to the host rock indicating a reduction in grain size due to cataclasis (Fig. 8) (Fossen et al., 2007; Balsamo et al., 2010). The median grain equivalent circular diameter in deformation bands is 37 µm compared with 57 µm in the host rock, showing a 35% reduction (Fig. 8). Deformation bands also show a smaller range in grain size at 156 µm compared to 231 µm in the host rock, with the host rock preserving larger grains. Deformation bands, compared to the host rock, are characterised by a high matrix content, due to grain size reduction, and a concentration of clay minerals permitting the distinction between the two (Fig. 7). The amount of matrix decreases from the centre to the outside of the bands and becomes almost non-existent in the host rock which is dominated by intact grains, with/without intragranular fractures, and pore space. There is an average absolute porosity reduction of 8% (from ca. 13% in the host rock to ca. 5%) in deformation bands (Fig. 9). This equates to 59% relative porosity reduction. Relict medium-sized pores (30-50 µm) are present within some bands, accounting for much of the remaining ca. 5% porosity. Quartz overgrowths are present in the host rock and deformation bands indicating active pressure-dissolution during the deformation history (Fig. 7). Overgrowths are not abundant, yet they do contribute to the reduction in pore space. Using porosity reduction as a proxy for inelastic volumetric strain, we obtain a ratio of D_S/D_C of 65 on average indicative of CSBs (Soliva et al., 2013; Ballas et al., 2014; Soliva et al., 2016; Fossen et al., 2018). Grain fracture is observed at grain contacts and within grains in both host rock and in deformation bands (Fig. 7). The microfracture density is greater in the host rock than in the deformation band. On average, 8.5 fractures/mm^2 are observed in host rock compared with 2.4 fractures/mm^2 in the deformation bands. Host rock microfracture density was measured within the same thin section as deformation bands, and therefore, is not representative of the entire unit. The presence of microfractures in the host rock shows that the deformation is not solely concentrated within deformation bands. Due to a reduction in grain size, a significant reduction in porosity and a low density of microfractures, D2 deformation bands are classified as *cataclastic* CSBs (Antonellini et al., 1994; Mair et al., 2000; Fossen et al., 2007; Ballas et al., 2015).

465
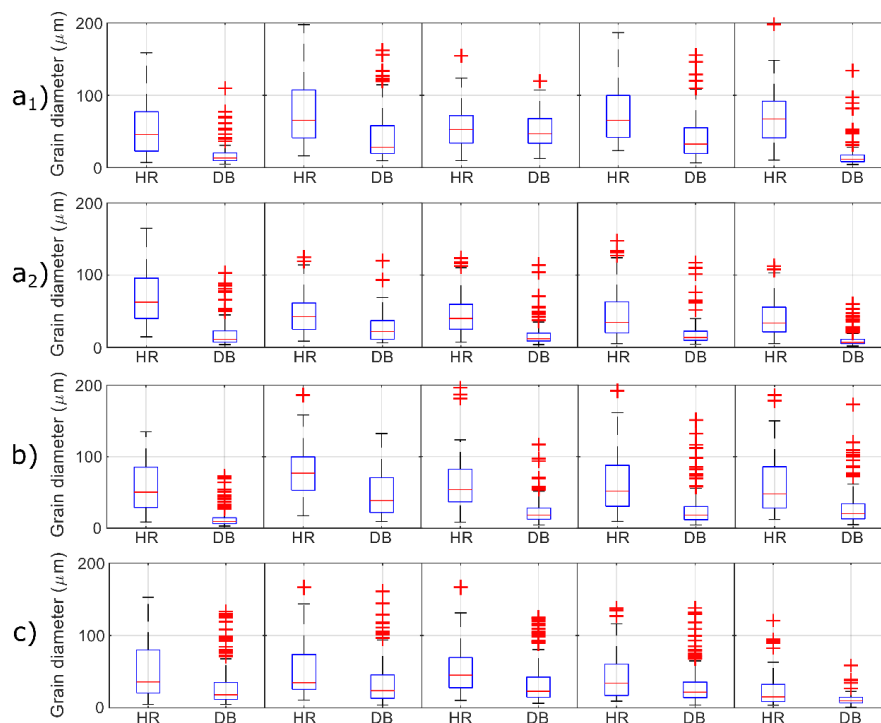
Figure 8. Box and whisker plots to show the difference in grain size distribution in deformation bands compared to host rock. a$_1$ & a$_2$) Grain size distributions associated with deformation bands located in D2 fault damage zones. b) Grain size distributions associated with deformation bands located in D3 fault damage zones. c) Grain size distributions associated with D3 non-FDZ deformation bands. For each sample, the interquartile range and the median are smaller

470 **in the deformation bands compared to the host rock. The tops and bottoms of each box are the 25th (Q1) and 75th (Q3) samples, respectively. The centre line represents the median. The whiskers are drawn from the ends of the interquartile ranges to the adjacent values (Q1 - 1.5 * interquartile range and Q3 + 1.5 * interquartile range). Data that lies beyond the whisker length are outliers (red crosses).**
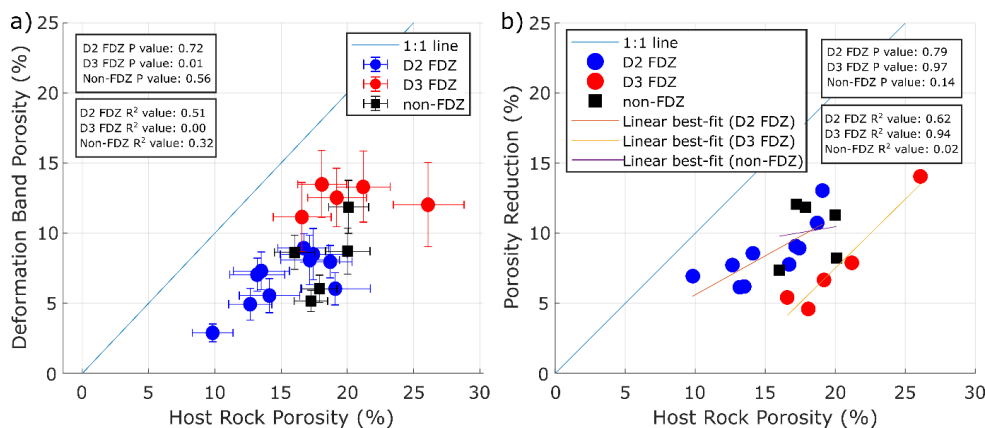
Figure 9. a) Measured host rock porosity % plotted against porosity measured in the deformation band (%). Each data point represents a thin section where porosity was measured in host rock and deformation band. All deformation bands exhibit a reduction in porosity compared to the host rock. b) Host rock porosity (%) plotted against the absolute reduction in porosity. The linear fit for the data in b) shows that the reduction has a positive correlation with the host rock porosity. *P-value* **= Pearson correlation coefficient value. Raw statistical data are shown in Supplement Section S.7.**

4.4. D3 Horizontal Contraction

4.4.1. Structures and Relative Timing

Field overprinting criteria show that a contractional event followed D2 horizontal extension (Fig. 5) (Chanier et al., 1999). Macro-scale D3 overprinting relations include: folding-induced dissection of D2 faults at bedding interfaces through flexural shear of and slip along weak mudstone layers; multiple generations of slickenfiber veins in D2 faults where strike-slip orientations overprint dip-slip ones; cross-cutting of D2 faults by D3 thrusts – easily observed along the coast (also observed at the deformation band scale); rotation of D2 faults around D3 fold hinges (Fig. 5). These relations have also been described by Chanier et al. (1999) for the North Island east coast.

The structures associated with D3 are: [1] folds; [2] reverse faults; [3] reverse-sense deformation bands located in the damage zones of faults; and [4] deformation bands with constant spacing and minimal to no offset. Field overprinting criteria cannot be used to discern the relative timing of these structures during this contractional phase as all structures are not seen interacting in a single outcrop.

4.4.2. Faults and Folds

Upright, NE-SW trending folds with 100 m-scale wavelengths and along-strike extents of several km's constitute the most obvious large-scale D3 structures (Fig. 1). Fold axes are shallow and doubly plunging NE and SW (Fig. 2). Unlike D1 folds, D3 folds are asymmetrical, with steeper eastern limbs and non-cylindrical geometry (Fig. 1). Synclines commonly have open hinges and resemble box folds in their geometry. Anticlines resemble kink folds with closed hinges and long straight limbs. Higher-order parasitic folds with matching geometry are observed throughout the mapping area and best exposed in road cuts in the hinterland. Within fold limbs, layer-parallel slip and shear can be observed in interbedded mudstone layers, along with thinning-out of these layers. Slip surfaces with slickenfiber veins exhibit opposing shear sense on opposing fold limbs. These observations could be associated with both bending and buckling folding mechanisms (Donath and Parker, 1964; Chapple and Spang,

1974). Given the fact that D3 axial planes trend parallel to the traces of the dominant thrust faults in the area, it is reasonable to assume, by assessing the poles to the axial planes, that D3 folds formed by SE shortening (Grujic and Mancktelow, 1995). This is consistent with the shortening direction indicated by regional thrust faults (Chanier et al., 1999). While D1 fold geometry is inconsistent with D3 fold geometry, field observations cannot confirm whether D3 folds nucleated during D1 and tightened during D3 or whether they nucleated and tightened throughout D3.

D3 reverse faults can be observed along the coastline (Fig. 1, Fig. 6). Poor hinterland exposure prevents their observation away from the coastline. Fault length is often indiscernible as they extend beyond cliff height (>10 m). However, some are shorter than the cliff face (<10 m in length). Fault displacement ranges from 0.2 m to 5 m and is ca. 1 m on average. Reverse faults trend NNE-SSW with an average dip of 48°. A dominant set dips ESE, and a secondary set dips WNW. Statistical analysis shows that the fault orientations are not distributed bimodally (Healy and Jupp, 2018). D3 reverse faults are brittle structures with cataclastic fault cores and occasional gouge. Paleostress analysis of back tilted D3 reverse faults with slickenfiber veins and shear sense is consistent with the literature and is in alignment with the present-day movement of the Pacific plate (σ_1: 01/092°) (Fig. 2) (Chanier et al., 1999; Bailleul et al., 2013). We have analysed back-rotated D3 faults because deformation bands in the damage zone of these faults mutually crosscut conjugate D3 bands with no apparent offset, and orientation analysis of the latter shows that they have been passively rotated during folding (see Supplement Section S.4). However, we cannot rule out that faulting could have occurred anytime during D3, especially in steep fold limbs when deformation can no longer be accommodated by folding. We do not have evidence for this as most of the fieldwork took place at coastal outcrops that were in the gentle to moderately dipping back-limb of a syncline.

4.4.3.   Deformation Bands

When comparing dihedral angle and D_S/D_C ratio, two types of deformation bands are associated with D3: reverse-sense CSBs and SECBs. SECBs are the most common.

4.4.3.1.   D3 SECBs

SECBs are mainly hosted in regions dominated by sandstone, with less interbedded mudstone. SECBs primarily form single bands but also occur in narrow clusters in areas with higher band densities. On average, single bands are 5 mm in width with a range from 0.26 mm – 1 cm. Clusters are on average 2 cm wide. Eye and ramp structures can be recognised in the networks. The bands are lighter in colour than the host rock and show positive relief (Fig. 6). SECBs exhibit no observable shear displacement, except where clusters are present and millimetre offset can be observed. Some bands pass through multiple beds and can extend beyond the scope of observation. Most commonly, however, SECBs are confined to individual sand- and siltstone beds where they form two sets of bands trending NNE (Fig. 2, Fig. 6). Overprinting relationships show that commonly one of the two sets predates the other. From 11 analysed outcrops back tilting of deformation band orientations results in tighter clustering in Schmidt nets, suggesting that SECBs formed before folding initiated. In addition, bands orientations mapped on the same bed across a fold hinge lie on the same great circle suggesting that these bands predate D3 folding (see Supplement Section S.4). Pattern analysis shows that most SECBs have a bimodal orientation distribution and can be considered as conjugate sets (Healy and Jupp, 2018). The average dihedral angle is 82° (after back-rotation), ranging from 68-89°.

Microscopically, SECBs have diffuse borders with the surrounding host rock. The bands are characterised by a reduction in grain size and porosity (Fig. 7). Host rock median grain size is 39 µm and deformation band median grain size is 22 µm, representing a 44% reduction (Fig. 8). The range in grain diameters inside and outside of the

545   bands is similar: 157 µm for deformation bands and 162 µm for host rock. However, the interquartile range is much less for deformation bands: 49 µm for host rock and 27 µm for deformation bands. This small range for deformation bands results in many outliers indicating relict, less fractured grains are present within the bands (Fig. 8). Grain size within the bands has a unimodal, positively skewed distribution, indicating cataclasis with a larger number of smaller grains. Positive skew suggests that not all grains have been equally fractured. The porosity

550   within the deformation bands, on average, reduced from 18.5% in the host to 8.8%, a relative reduction of 52% (Fig. 9). Quartz overgrowths are observed around grains in the host rock and deformation bands. Like D2 bands, microfracture density is high in the surrounding host rock, 6.3 fractures/mm^2 in the host rock and 3.8 fractures/mm^2 in the deformation bands. Within the bands there is a cataclastic fine-grained matrix, which is generally absent in the host rock. Analysis of compaction versus shear shows an average D_S/D_C value of 0.83 for

555   SECBs, ranging from 0.2 – 1.5. This value shows that compaction and shear magnitudes are similar, and the bands are therefore microscopically classified as cataclastic SECBs.

4.4.3.2.   D3 CSBs

D3 reverse-sense CSBs are dominantly observed within the damage zone of reverse faults. However, bands are also observed away from faults. While in fault damage zones all bands have the same dip direction, two sets of

560   CSBs with opposing dip are observed away from faults. CSBs are very similar in macroscopic appearance to SECBs with high relief and lighter colour compared to the host rock. However, fault-related CSBs resemble D2 CSBs when clay smear is present (Fig. 6). They mainly occur as single bands but also in clusters. Single bands are on average 5 mm wide and range from 3 – 7.5 mm. Clusters are ca. 2-3 cm in width (Fig. 6). CSBs accommodate mm-cm scale reverse offset. The bands trend NNE with one poorly clustered dominant set dipping

565   ESE (Fig. 2). The dominant set dips ESE at 63° and the less dominant set dips WNW at 29°. This orientation data is very similar to D3 faults indicating that they formed in the same stress state. SECB orientation does not match with fault orientation as strongly (Fig. 2). The bands generally propagate for multiple meters and extend out of outcrop observation, not unlike D2 normal sense deformation bands. However, some are truncated against thicker mudstone intervals. Pattern analysis rejects bimodality in CSBs associated with faults, suggesting a polymodal

570   orientation distribution (Healy and Jupp, 2018). However, CSBs observed between faults, similarly to SECBs, are bimodal with dihedral angles ranging from 51-80°.

Microscopically, CSBs are characterised by diffuse edges (Fig. 7). These bands show the largest reduction in grain size of all deformation bands observed at the field site. Median host rock grain size is 57 µm compared to 21 µm in the deformation bands, a reduction of 63%. The total range in grain size is similar for the host rock and

575   deformation bands, 228 µm for the host rock and 224 µm for the deformation band. However, the interquartile range is considerably different, 54 µm for host rock and 22 µm for the deformation band. This variation is similar to that seen in the D3 SECBs. As with the other bands, D3 CSBs have a lower porosity than the host rock, 20% outside of the band and 12.3% inside the band – a reduction of 39% (Fig. 9). This is the smallest reduction in porosity observed across the varieties of deformation band. Pore space in deformation bands is filled with

580   fragments of grains, clay, and quartz overgrowths. Quartz overgrowths have also reduced host rock porosity. Grains within the bands and the host rock show intragranular fractures radiating from grain contacts (Fig. 7).

There is a higher density of microfractures in the host rock surrounding the bands, as is observed in normal CSBs and SECBs. Microfracture density in the host rock is 6.3 fractures/mm^2, while the density in the deformation bands is 3.1 fractures/mm^2. Compaction and shear analysis shows that the Ds/Dc value is 63 ranging from 32 –
585   106. This, as with D2 bands, indicates considerably more shear strain and characterises the bands as CSBs.

4.4.3.3.   Proto-Deformation Bands

Host rock surrounding D2 normal-sense CSB bands and both types of D3 deformation bands, reverse-sense CSB and SECB, is characterised by pockets of cataclastic material that can be observed to originate from the crushing of individual grains. Throughout thin sections, these pockets can be seen to align with the same orientation as the
590   deformation bands (Fig. 7).

4.5.   Spacing

4.5.1.   Synthetic Spacing

To explain the spacing analysis of natural data, six synthetic images representing different spatial distributions of deformation bands were constructed (Fig. 10). Bands with a strictly constant spacing show a zero Pearson
595   correlation coefficient (Fig. 10). With the addition of normally distributed 'noise' to case [a], a distributed set of spacing with Gaussian noise is obtained (Fig. 10). In this case [b], the Pearson correlation coefficient of spacing over distance is -0.08. The third synthetic image [c] represents a damage zone with exponential decay of deformation band density away from the fault plane. For this example, the Pearson correlation coefficient between spacing and distance to fault is exactly 1 (Fig. 10). A histogram of this spacing distribution shows positive skew.
600   The same results are expected for any other analytical expression in which spacing grows monotonously with distance from the fault e.g.: the power-law relationship established by Savage and Brodsky (2011). With the addition of Gaussian noise to a damage zone [d], the Pearson correlation coefficient reduces to 0.56. However, its exact value depends on the amount of noise and can be larger or smaller. Synthetic image [e] represents an overprint of two distributions, equal spacing and variable spacing, simulating two different deformation events
605   affecting the same bed subsequently. If the deformation bands resulting from the two events are morphologically similar, they may be difficult to distinguish between in the field and can be mapped together as one. In this case, the Pearson value is 0.71, although it could be any value between 0 and 1 dependent upon the value of spacing in the background density compared with the damage zone spacing. In image [f], noise is integrated into both distributions and they are combined. This is the most realistic outcome if there is an overprint of two events with
610   different distributions. In the case shown the Pearson value is 0.59, however, with different magnitudes of noise and varied initial spacings, any value from -1 to 1 could be obtained. For the interpretation of our field data, we assume a positive correlation between band spacing and spatial location if the Pearson value > 0.5.
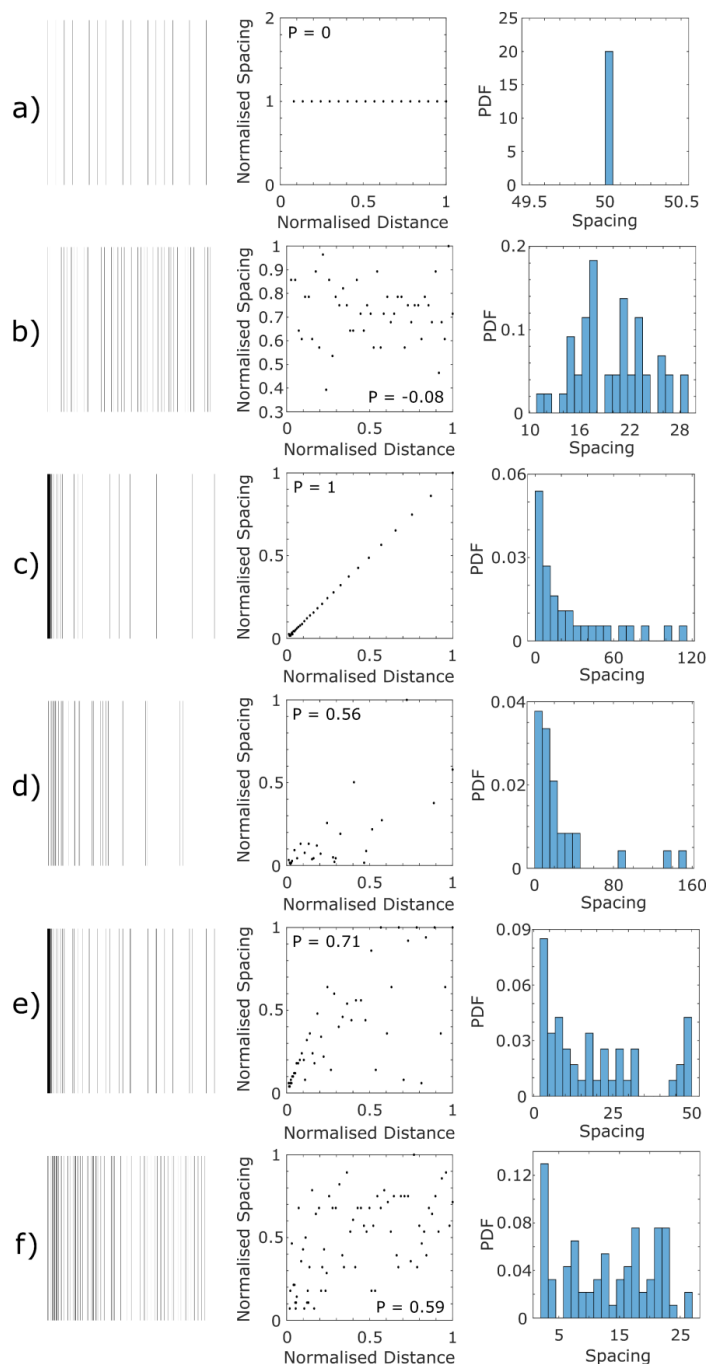
Figure 10. Synthetic images produced to replicate different distributions of the deformation band. (a) deformation bands with a constant spacing, (b) deformation bands with a constant spacing with added Gaussian noise, (c) bands with an exponential decay away from a fault plane, and (d) deformation bands with an exponential decay away from a fault plane with added Gaussian noise. (e) and (f) represent images that combine constant spacing with a damage zone. These examples would be relevant if a damage zone overprinted a constant background spacing of the deformation band. (e) combines (a) with (c). (f) combines (b) and (d) resulting in a spacing that contains two distributions that have

615

620   noise. The relationship between spacing and distance is analysed using the Pearson correlation coefficient. Values close
       to 1 show a positive relationship between the distance from a point and the spacing. This would be seen in a damage
       zone that shows an increase in spacing between deformation bands as the distance from the fault plane increases.
       Pearson correlation coefficient values close to 0 show no correlation between spacing and distance. A histogram of the
       spacing is also shown. Unimodal distributions with no skew reflect bands with near-constant spacing. A positive skew
625   represents damage zones. Distance and spacing are also plotted for different scan-lines. Distance is normalised to the
       maximum distance and spacing is normalised to the maximum spacing. P = Pearson correlation coefficient value.

4.5.2.   Natural Spacing

4.5.2.1.   Map Scale

Analysis of the location of these macro-scale faults, with displacements greater than 20 cm, show that many have

630   a similar spacing (Fig. 11). D2 faults have a positively skewed distribution with a skewness value of 0.3. Median

spacing is 8.7 m when corrected for true spacing. The Pearson correlation coefficient for the spacing against

distance is -0.07, with an analysis conducted from SW-NE. D3 faults have a bimodal distribution indicating two

primary spacing populations with modes of 5 m and 13 m when corrected for true spacing. Skewness for D3 faults

is 0.03. The Pearson correlation coefficient is 0.44. Pearson values < 0.5 indicate that there is no correlation

635   between the spacing and location of normal or reverse faults.
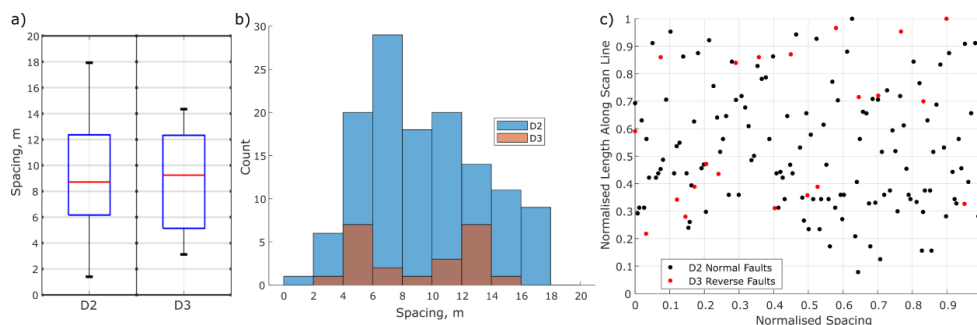
**Figure 11. (a) Boxplots of corrected spacing distribution of D2 normal faults and D3 reverse faults. (b) Histograms of
the corrected spacing distribution of D2 normal and D3 reverse faults. A normality test (Lillie test (Mathworks, 2011))**
640   **shows that D2 has a normal distribution while normality is rejected for D3. D2 shows a positive skew, and D3 has a
bimodal distribution. (c) The plot of the normalised spacing against distance from the start of the scan-line for normal
and reverse faults. The plot most closely resembles (b) and (f) from Figure 10.**

4.5.2.2.   Deformation Band Spacing

Qualitatively, deformation bands in the mapping area appear to exhibit two spacing distributions. Generally, those

645   associated with faults (both normal- and reverse-sense) form fault damage zones with a variable distribution (Fig.

6**Error! Reference source not found.**) where spacing increases with distance from the fault plane. Damage zone

width varies greatly along faults and from fault to fault. Some damage zones can extend for up to 5 m before

interacting with the damage zone of an adjacent fault, while other beds along the same fault show no macroscopic

damage zone. The second spatial distribution is a regular spacing. Regular spacing is generally observed when

650   there is no fault nearby. Regularly spaced bands are also observed in damage zones as a separate signal to bands

with variable spacing. Quantitatively these observations were tested with the hypotheses: bands observed adjacent

to a fault plane have a positive correlation between spacing and distance from the fault plane and bands not

observed adjacent to a fault plane have no relationship between spacing and distance.

4.5.2.2.1.   Fault Damage Zone Deformation Bands

655   D2 normal and D3 reverse faults are bordered by deformation bands, forming a fault damage zone. Damage zone
width varies from 0.1 cm to 272 cm for the analysed faults with associated thin section analysis. The damage zone
width was measured between the outer deformation bands that shared the orientation of the fault. Twelve faults
with damage zone width > 10 cm were analysed for spacing statistics. The average Pearson correlation coefficient
for each analysed fault ranges from 0.07 to 0.62 with a combined average of 0.4 (see Supplement Section S.8 Fig.

660   S8.4). 71% of D2 and 60% of D3 FDZ spatial distributions have Pearson coefficient distributions with a median
< 0.5 indicating that there is no correlation between spacing and distance (see Supplement Section S.8 Fig. S8.4).
Analysis of spacing distributions shows that all faults have positively skewed spacing values (see Supplement
Section S.8 Fig. S8.6). This data most closely matches synthetic images (d) and (f) indicative of a damage zone
or spatial overprints.
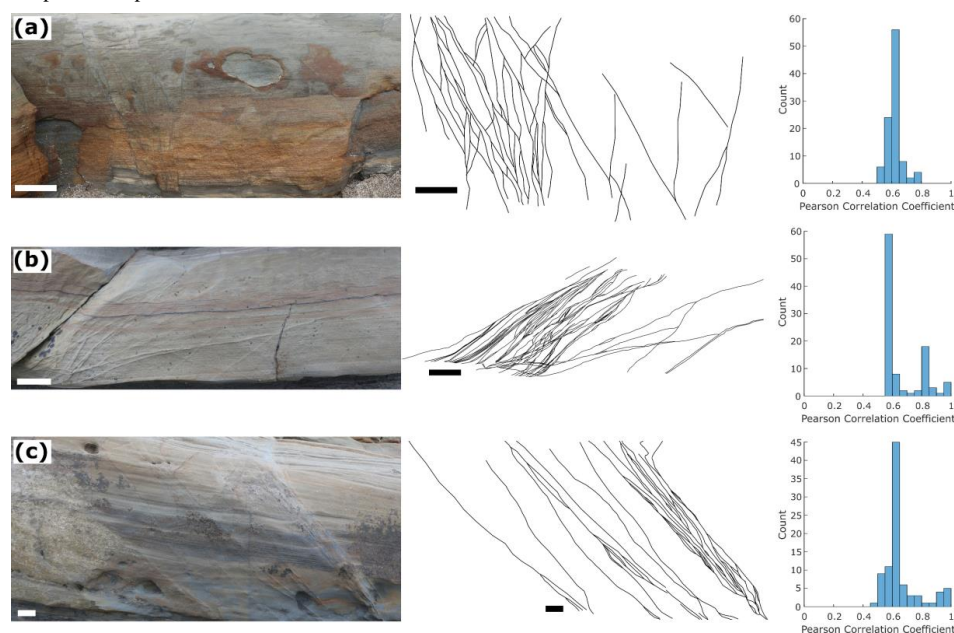
665

Figure 12. Spacing analysis of CSBs associated with the damage zone of faults. The scale bar is 10 cm for all images. 100 scan-lines were taken for each image during analysis. (a) represents a D2 normal fault and (b) and (c) show small D3 reverse faults. Each of the three faults show an increase in spacing between deformation bands with increasing distance from the fault plane. This is reflected in the Pearson correlation coefficient. Values are approaching 1, which
670   **shows a dependence of distance on spacing.**

4.5.2.2.2.   Non-FDZ Deformation Bands

We examined D3 SECBs and CSBs with apparently constant spacing from twenty-eight outcrops where damage
zones were not clearly detected, and fault planes were at least 3 m away. The spacing generally does not correlate

675   with distance from the first deformation band (Fig. 13). Many peak Pearson correlation coefficients are close to
0, average of 0.02, with a normal distribution indicating no relationship between spacing and distance (Fig. 13).
However, Pearson values range from -0.65 to 0.61, indicating that there are outcrops at least 3 m away from faults
that show a distance control on spacing (see Supplement Section S.8 Fig. S8.5). 10% of analyses are complex

with strongly skewed spacing frequency distributions and Pearson coefficient values indicative of control on
680   spacing (>|0.5|) (see Supplement Section S.8 Fig. S8.7). 43% of analysed outcrops, however, show variable
Pearson values as the scan-lines analyse different regions of the outcrop. Large ranges of values are observed, and
in some cases these values are negative, indicative of an anticorrelation between spacing and distance. This effect
can be seen in Figure 13c where a scan-line along the top of the image would result in a negative Pearson value,
as observed in the Pearson histogram (Fig. 13). This highlights the importance of using multiple scan-lines. Data
685   for bands not associated with faults correlates with synthetic images [2] and [6], corresponding to constant spacing
with 'noise' and overprinted distributions, respectively. Discrete spacing values range from 1.4 cm to 14.8 cm.
Equivalent outcrops with D2 bands were not analysed for spacing statistics as suitable outcrops were proximal to
faults and, therefore, did not meet the criteria.
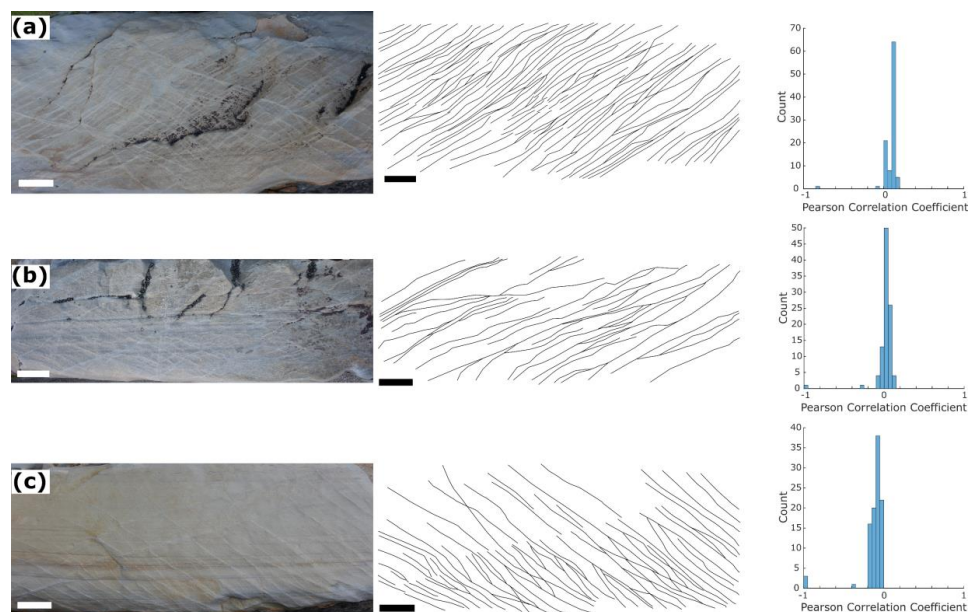
690   **Figure 13. Spacing analysis of dominantly SECBs with rare CSBs not associated with the damage zone of faults. The
scale bar is 10 cm on all images. 100 scan-lines were taken for each image during analysis. Each image shows a general
lack of correlation of the distance with the spacing between deformation bands. Pearson correlation coefficient values
close to 0 further suggest a lack of correlation. These bands show a near-constant spacing.**
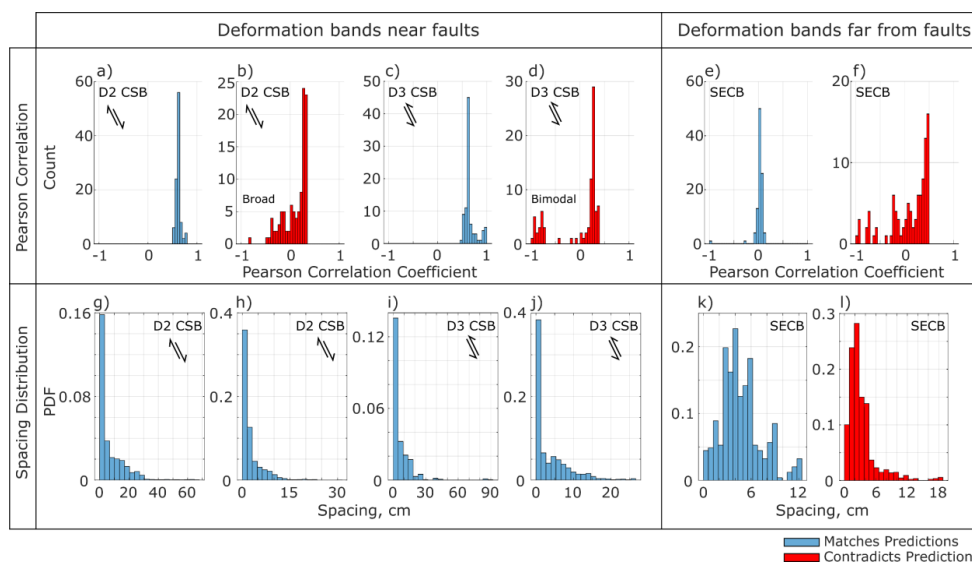
695   **Figure 14. Spacing statistics for selected outcrops to highlight the variation in deformation band distribution across the field site. The figure has been separated into bands that were analysed adjacent to normal- and reverse-faults, where a decay of spacing away from the fault plane is expected, and those that were analysed away from fault planes where no correlation between spacing and distance is expected. Two examples of each have been chosen to represent possible end-member datasets. a-f show distribution of Pearson correlation values for each analysed scan-line for the outcrops.**

700   **CSBs are primarily associated with faults and are expected to show a positive correlation (Pearson > 0.5). SECBs, with some conjugate CSB sets, were measured > 2 m from faults and should not show a correlation between spacing and distance resulting in a Pearson value close to 0. a, c, and e show examples that match these predictions. b, d, and f are examples that contradict these predictions. g-l shows the spacing frequency distributions for different outcrops. Band spacing associated with faults is expected to show a positive skew. All bands associated with faults show a positive skew.**

705   **However, variation can be seen with large ranges and a non-smooth curve. Bands not associated with faults are expected to show a Gaussian distribution, representing a 'regular' spacing with noise (Fig. 10b). k shows this while l is characterised by a positive skew, as would be expected for a fault damage zone. Data for all analysed outcrops can be observed in Supplement Section S.8.**
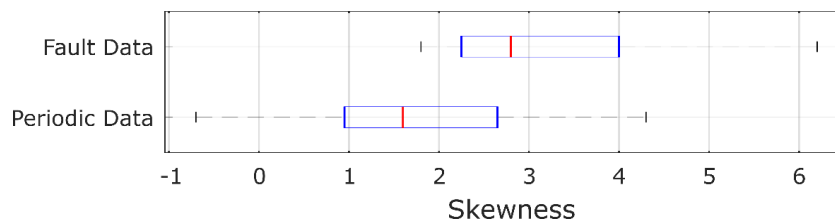
710   **Figure 15. Boxplots showing the frequency distribution of skewness values for the spacing distribution of deformation bands in fault damage zones and those located not adjacent to a fault (non-FDZ data). Periodic data shows less skew (0 being normally distributed). This correlated with synthetic images from Figure 10 showing regular spacing with noise. Fault data has a higher skew which also correlates with Figure 10 showing a damage zone with additional noise.**

5. Discussion

715   In the following, we will discuss how our observations of deformation bands from Castlepoint, New Zealand compare with previous studies and if similar relations to the tectonic regime are observed. We shall first discuss the association of tectonic regime with deformation band kinematics, and spatial distribution of bands before we conclude with a brief remark on implications for fluid flow in this deformed rock sequence.

5.1.   Band Kinematics, Orientation, and Microstructure

720   Outcrop and microstructural data demonstrate that D2 bands, associated with a normal-fault regime, are dominantly CSBs with rare SECBs. SECBs are identified by their lack of offset and higher angle to σ_1. In other extensional regimes, only CSBs and Shear Bands (SBs) are observed (Soliva et al., 2013; Ballas et al., 2014; Fossen et al., 2015; Soliva et al., 2016; Fossen et al., 2018). SECBs are not predicted to form during normal faulting because smaller mean stresses and larger differential stresses are expected compared to a thrust-fault

725   regime where SECBs are commonly observed (Soliva et al., 2013; Fossen et al., 2018). However, SECBs associated with extension are observed in a carbonate host rock where bands formed during deposition as overburden was increasing (Lubiniecki et al., 2019). Since the Whakataki Formation was still compacting and lithifying during D2 (Chanier et al., 1999; Bailleul et al., 2013), D2 SECBs in our research area may also be explained in this way. Extension-associated bands from Utah and Provence formed post-lithification and were

730   deformed in a tectonic stress state where the overburden, and hence, the vertical tectonic stress σ_v, are assumed to be constant for the duration of deformation (Solum et al., 2010; Soliva et al., 2013; Ballas et al., 2014; Soliva et al., 2016). However, since normal faulting in our study area was accompanied by ongoing sedimentation, increasing mean stress and diagenetic expansion of the yield envelope could have caused the yield envelope to be intersected closer to the cap and thus explain the presence of SECBs in an extensional regime in the Whakataki

735   Formation. In addition, if the initial stress path for D2 intersects the yield envelope close to the transition between SECBs and CSBs, only small variations in the stress state are required to move from one structure to another.

D3 thrust-fault-associated bands are dominantly SECBs with some CSBs, which is consistent with observations from other contractional regimes (Ballas et al., 2013; Soliva et al., 2013; Ballas et al., 2014; Fossen et al., 2015; Fossen et al., 2018). D3 bands mainly show a bimodal orientation pattern. However, when CSBs are in the vicinity

740   of faults, they are commonly unimodally oriented, with all bands sharing a similar dip to the main fault plane. Whether the pattern is symmetric or asymmetric in the thrust-fault regime depends on the elastic properties of the layers and the friction coefficient between layers (Chemenda et al., 2014). Heterogeneity in the Whakataki Formation results in variable material properties which in some places may favour symmetry, and in others asymmetry. In addition, as a bed experiences progressive deformation, material properties change as well, and

745   transitions from asymmetry to symmetry can also occur (Saillet and Wibberley, 2010; Klimczak et al., 2011; Chemenda et al., 2014).

Microstructurally, all bands are characterised by a reduction in porosity and grain size, which is consistent with literature for bands formed in normal- and thrust-fault regimes (Solum et al., 2010; Ballas et al., 2013; Soliva et al., 2013; Ballas et al., 2014; Fossen et al., 2015; Fossen et al., 2018). The absolute average porosity reduction of

750   ca. 10% observed in all deformation bands from the Whakataki aligns with previous studies (Fig. 9). Permeability was estimated from porosity values using an empirical relationship (Wu, 2005) (see Supplement Section S.6). A comparison of host rock and deformation band reveals a reduction of ca. two orders of magnitude for the normal- and thrust-fault regimes. These values are within the bounds observed in previous studies (Ballas et al., 2015; Fossen et al., 2018).

755   Pattern analysis of orientation data reveals two distributions: [1] polymodal data associated with faults and CSBs and [2] bimodal data associated with SECBs and CSBs not associated with fault damage zones. Polymodal patterns are consistent with 3D strain, while bimodal patterns are consistent with the 2D plane strain (Fossen et al., 2018; Healy and Jupp, 2018; Cai, 2019). The 3D strain is most commonly expected in nature (Healy et al.,

2015; Healy and Jupp, 2018). We propose that the presence of a bimodal distribution in our data is a consequence

760   of the measurement scale. Orientations of faults and associated CSBs were measured over a large area at the kilometre scale. At this scale, deformation is 3D in the research area, as seen qualitatively by the variability in the large-scale fold and fault geometry (Fig. 1). In contrast, conjugate SECBs and CSBs were documented in a much smaller area on the scale of hundreds of meters because of outcrop conditions. On this scale, structures can be fairly cylindrical (Fig. 1), and there is a higher chance to sample at a plane-strain scale. At the km-scale, there are

765   many physical reasons for expecting 3D strain in D2 and D3 structures of the Whakataki Formation: [1] the layers have already been folded and faulted in D1 horizontal contraction; [2] the Whakataki Formation has along-strike and stratigraphic thickness variations; [3] rough seafloor topography below the wedge, combined with oblique subduction can induce strong stress/strain heterogeneity (Jones et al., 2005; Wang and Bilek, 2014); [4] the stress field evolved gradually with the principal stress orientations rotating in the transition from D2 (vertical σ_1) to D3

770   (horizontal σ_1); [5] faults locally perturb the stress field and generate heterogeneous orientations (Maerten et al., 2016); and [6] the material properties in different layers can be anisotropic. All of these effects should result in spatial and temporal differences in stress state on a variety of length scales. Therefore, one can expect the contemporaneous formation of bands with quite different kinematics, possibly explaining the presence of CSBs and SECBs in both normal- and thrust-faulting regimes and complex patterns in outcrop.

775   ### 5.2.   Deformation band spatial distribution

In the Whakataki Formation, deformation bands with a regular spacing, and deformation bands localised into zones and clusters are observed in normal- and thrust-faulting tectonic regimes. The observation of regularly spaced bands associated with a normal-fault regime contrasts with previous studies that identified a tendency of localisation, not pervasively distributed deformation bands (Soliva et al., 2013; Ballas et al., 2014; Fossen et al.,

780   2018). Regularly spaced bands have only been observed in extensional settings when associated with; [1] large relay ramps, [2] when deformed layers are above soft layers such as shale or salt, and [3] when forming in large rollover structures (Fossen et al., 2018). The Whakataki Formation most closely resembles case 2, with deformed strong sandstone beds embedded in soft mudstone layers. However, our observation is on a smaller scale than that suggested by Fossen et al. (2018). Conversely, in a thrust-fault regime, previous studies documented more evenly

785   distributed bands (Soliva et al., 2013; Ballas et al., 2014; Soliva et al., 2016; Fossen et al., 2018). Variably spaced CSBs and SBs in clusters are rarely observed in the contractional regime, and only when associated with faults (Ballas et al., 2014; Ballas et al., 2015; Soliva et al., 2016; Fossen et al., 2018). In the Whakataki Formation, pervasively distributed deformation bands are documented for normal- and thrust-fault regimes, with localisation occurring in the vicinity of faults in both cases. Of the twelve faults studied here, only 29% of damage zones

790   associated with a normal fault regime and 40% associated with a thrust fault regime exhibit a positive correlation between CSB spacing and distance from the fault plane. In the thrust fault regime, 90% of outcrops away from faults show no correlation between the band spacing and distance. In total, only seven of the forty studied outcrops are characterised by a clear positive correlation between spacing and distance. Therefore, both horizontal extension and contraction involve the pervasive formation of distributed CSBs and SECBs. Both stress regimes

795   also come with localised damage-zone-type CSBs. In summary, our field observations show a less distinct difference in the spatial distribution of deformation bands as documented previously for normal- and thrust-faulting regimes (Soliva et al., 2013; Ballas et al., 2014; Fossen et al., 2018).

The recognition of deformation bands with regular spacing near faults is based on our interpretation of the statistics of Pearson correlations. Where we observe bimodal or very broad distributions of Pearson coefficients, the spacing
800   distribution is interpreted to reflect progressive deformation and/or multiple tectonic events that have superposed different generations of deformation bands with similar attributes (Fig. 14). This seems to be the most common case in our research area and can be explained with the following conceptual model.

We propose that in the early stages of horizontal extension and horizontal contraction, pervasively distributed CSBs and SECBs form (Fig. 16). The local orientation, spacing, and kinematics of individual bands in this early
805   stage of distributed strain depend on the highly variable rheological properties of the sedimentary layers, layer thickness, and the orientation of the layers relative to the far-field stress (Gross, 1993; Knott et al., 1996; Martel, 1999; Bai and Pollard, 2000a; Bai and Pollard, 2000b; Olsson and Holcomb, 2000; Ackermann et al., 2001; Rudnicki, 2003; Soliva and Benedicto, 2005; Soliva et al., 2006; Chemenda, 2009; Laubach et al., 2009; Chemenda et al., 2012; Regenauer-Lieb et al., 2013a; Regenauer-Lieb et al., 2013b; Chemenda et al., 2014; Zuza
810   et al., 2017; Laubach et al., 2018). Our microstructural data demonstrate that there is no difference in the deformation mechanisms of CSB and SECB formation. Therefore, only small changes in the local stress state and yield envelope are required to move from one structure to another because the kinematic transition is continuous and simply reflects different degrees of shear displacement and volume reduction (Fossen and Bale, 2007). With continued strain, favourably located deformation bands can link across sedimentary layers and cause the
815   propagation and formation of throughgoing slip surfaces (Fig. 16) (Aydin and Johnson, 1983; Antonellini et al., 1994; Shipton and Cowie, 2001, 2003; Schueller et al., 2013). Many CSBs associated with immature small faults are sub-parallel to the fault (Figs. 2, 5, 6), which supports the idea that faults nucleate through linkage of deformation bands across layers. Moreover, at the regional scale, normal- and reverse-faults in the Whakataki Formation are uniformly distributed (Fig. 11). This is consistent with the idea that fault spacing is strongly
820   controlled by the mechanical stratigraphy of the turbidite stack (Knott et al., 1996; Martel, 1999; Ackermann et al., 2001; Soliva and Benedicto, 2005; Soliva et al., 2006; Laubach et al., 2009; Zuza et al., 2017; Laubach et al., 2018). Once throughgoing faults have formed, progressive slip is expected to cause the formation of the wall-, interaction-, and tip-damage zones (Kim et al., 2004; Peacock et al., 2017) that then overprint CSBs with a variable spacing (Shipton and Cowie, 2003; Faulkner et al., 2011; Xu et al., 2012; Maerten et al., 2016). In this scenario
825   of progressive deformation, one would expect a bimodal distribution of Pearson correlation coefficients where the mode that is close to zero reflects the initial band generation with regular spacing, and a higher mode > 0.5 reflects that of the damage-zone overprint. Moreover, there are many outcrops with distinct generations of cross-cutting structures associated with the same deformation phase as well as those where D3 structures overprint D2 structures. Broad distributions of Pearson coefficients may reflect outcrops that experienced overprint by three or
830   more distinct band-generating events (Fig. 14).
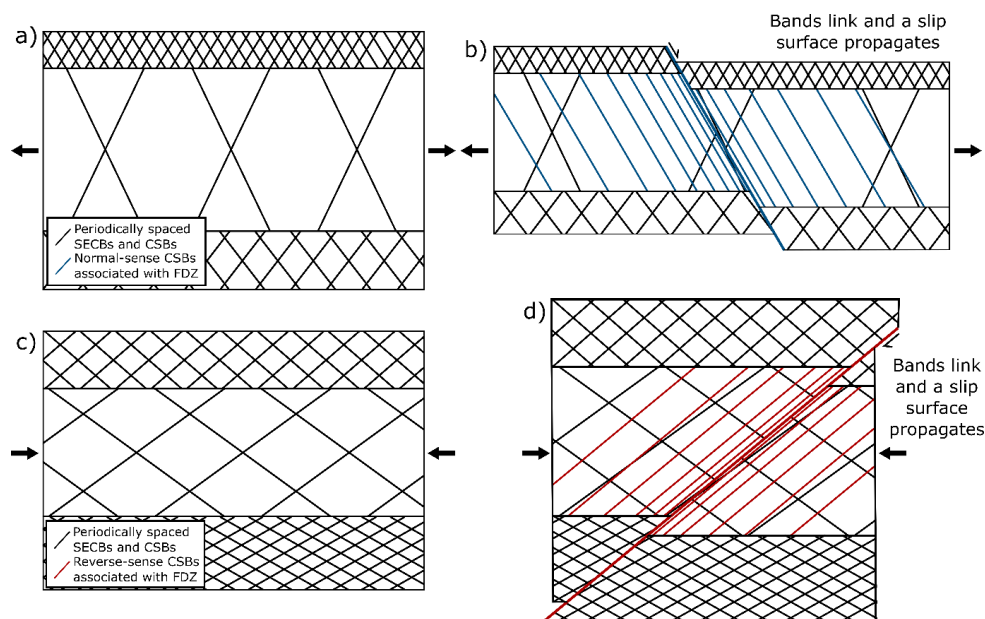
Figure 16. A schematic to show the evolution of spatial distributions in normal- (a & b) and reverse-faulting (c & d) tectonic regimes. Initially, bands with an equal spacing form. Band spacing is theorised to be proportional to the layer thickness, as is observed with joints (Pollard and Aydin, 1988; Gross, 1993). Eventually, bands link across layers and a fault propagates (Aydin and Johnson, 1983). The fault movement causes the local stress field to be perturbed resulting in new band formation with orientations and kinematics matching that of the new local stress field.

5.3.   Tectonic control and the stress path

Stress path modelling was employed in previous field studies to explain the kinematics and orientation of the observed deformation bands as a function of the tectonic regime (Saillet and Wibberley, 2010; Solum et al., 2010; Soliva et al., 2013; Ballas et al., 2014; Fossen et al., 2015; Soliva et al., 2016). We do not use this approach here because of the inherent complexity of the evolution of the state of stress within accretionary prisms. Critical wedge theory demonstrates that the state of stress in accretionary wedges is controlled by the geometry of the wedge (slope angle and dip angle of the subduction master fault), pore-fluid pressure, the frictional properties of the wedge, and the basal coefficient of the subduction thrust (Hu and Wang, 2006; Wang and Hu, 2006). The spatial distribution of seismicity along subduction faults implies that the wedge can be separated into a velocity-strengthening section (outer wedge) and a seismogenic velocity-weakening section (inner wedge) (Wang and Hu, 2006). This causes the inner and outer wedges to exhibit significant differences in the mechanical state during failure. The Whakataki Formation has travelled from the top of the outer wedge into the inner wedge and back to the surface. During this journey, the formation has experienced significant changes in a stress state, as clearly indicated by the broad structural inventory (Fig. 2). It is difficult to constrain this stress history from field observations. To emphasise this point, we recall that even within the inner wedge, one can obtain large vertical differences in stress regime, such as upper levels being under horizontal extension while lower levels of the wedge are simultaneously in horizontal contraction and vice versa (Hu and Wang, 2006). Stress regime in the accretionary wedge is largely controlled by the basal friction coefficient of the subduction thrust and the pore-fluid pressure. Both parameters cannot be constrained reliably throughout the Miocene from our field observations. Therefore, to generate a comprehensive estimate of the stress path of the Whakataki Formation, at

least 2D stochastic mathematical inverse modelling complemented by time-resolved geophysical data and strong geochronological constraints of basin and deformation history is required. This is beyond the scope of the current study.

860

However, one generic idea proposed in the literature surrounding stress path modelling may apply to our case study: during extension, the mean stress is smaller than during contraction, resulting in an intersection of the yield envelope closer to the top of the cap and thus the formation of CSBs (Soliva et al., 2013). In D2 extension we also dominantly observe CSBs. Regional studies demonstrate that the deposition of the Whakataki Formation most

865   likely lasted until the end of D2 (Bailleul et al., 2007). Therefore, the overburden stress probably increased throughout D2. During D3, sediment thickness reached its maximum, and additional thickening through D3 folding and thrust-stacking would have added to the vertical stress. It is, therefore, likely that the mean stress increased from D2 to D3. In addition, a change of the mechanical properties of sandstones from D2 to D3 can be expected, due to porosity reduction associated with ongoing compaction and cementation. These mechanical

870   changes are associated with hardening resulting in a bigger yield envelope during D3 (Fig. 17) (Fossen and Bale, 2007). The combination of higher mean stresses and a bigger yield envelope in D3 compared to D2 could explain why we also observe more CSBs during D2 extension and more D3 SECBs during D3 contraction (Fig. 17), as proposed by Soliva et al. (2013), Ballas et al. (2014) and Soliva et al. (2016). This idea is certainly appealing in its simplicity. However, it remains to be tested with an inversion of the effective stress path for our study area,

875   which is a challenging problem. Finally, while a static yield model can explain the critical stress state required for failure and the resulting failure angle and deformation band kinematics, it provides no information on the timing, rate of failure, spatial distribution or the number of deformation structures (Zhang et al., 1990; Wong et al., 1992; Wong et al., 1997; Schultz and Siddharthan, 2005; Wong and Baud, 2012). Therefore, one cannot predict the spatial distribution of localised instabilities based on the static far-field stress and static yield envelope alone. Our

880   observations support the well-established notion that the mechanical stratigraphy plays a major role in determining the spatial distribution of faults and deformation bands in layered rock sequences (Knott et al., 1996; Martel, 1999; Ackermann et al., 2001; Soliva and Benedicto, 2005; Soliva et al., 2006; Laubach et al., 2009; Laubach et al., 2018). In this case, predictive models for the time and spatial evolution of deformation structures must resort to at least 2D mathematical forward modelling (Chemenda et al., 2014).

885
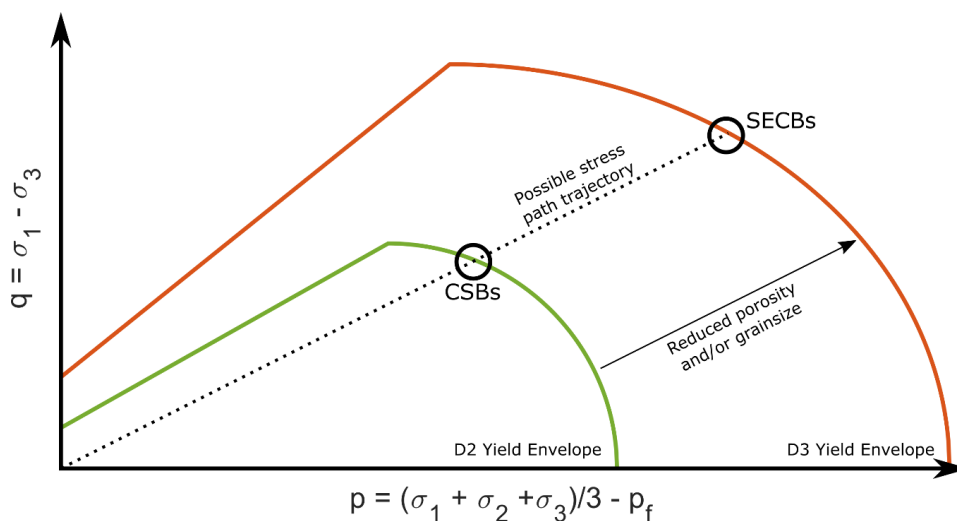
Figure 17. Schematic diagram of the potential yield envelopes for the Whakataki Formation during D2 horizontal extension and D3 horizontal contraction. During D2, the unit is still lithifying and being buried, therefore, in D3 when the unit has lithified, the yield cap has expanded (red line). For a generic increase in effective stress (p) and differential stress (q), the yield cap may be intersected at different points due to the evolution of the yield envelope through time. With only two points to constrain the stress path, there are many possible trajectories, all of which could result in the observed deformation band kinematics and distributions. In fact, the linear stress path shown here for illustration purposes cannot be correct because the stress regime in the Whakataki Formation switched at least two times (Soliva et al., 2013).

5.4.   Implications for fluid flow

Our field observations demonstrate that the heterogeneous sedimentary architecture, in concert with folds, faults, and deformation bands, transforms the Whakataki Formation into a complex reservoir that is strongly compartmentalised over four orders of magnitude in length scale. At the kilometre scale, some large folds and thrusts juxtapose rock formations with different petrophysical properties. At the 100- to 10 m scale, normal- and reverse faults dissect the Whakataki Formation into monoclinic or triclinic blocks with a dominant thickness of ca. 10 m. Faults can be both fluid conductors and inhibitors. However, D2 and D3 faults show lots of clay smear and gouge in our field area. Therefore, fluid flow inhibition is most likely (Fulljames et al., 1997; Yielding et al., 1997; Nicol and Childs, 2018). At the m- to dm-scale, interbedded mudstones can restrict fluid flow in sandstone layers in the vertical direction, resulting in an anisotropic hydraulic conductivity on the scale of metres to tens of centimetres. Finally, at the 10 cm-scale permeability-reducing deformation bands are observed in complex 3D networks (Antonellini and Aydin, 1994; Antonellini and Aydin, 1995; Fossen and Bale, 2007; Ballas et al., 2013), especially in the sand-rich facies. Thus, individual sand- and siltstone beds are subdivided yet again into even smaller blocks. In an accretionary prism where fluid is readily available, such compartmentalisation can result in high pore fluid pressures that may result in catastrophic failure of the wedge (Audet et al., 2009). For petroleum extraction, one may expect that hydraulic properties determined at the core scale are not representative of those at the reservoir scale. An integration of the multi-scale structural and sedimentary architecture with computational upscaling of flow properties is required for the prediction of reservoir properties (Field et al., 2006).

6. Conclusions

In conclusion, our study on deformation bands in the poly-deformed Miocene turbidites of the Whakataki
915 Formation provides the following key findings:

1. During extension, cataclastic CSBs form most frequently, accompanied by SECBs.
2. During contraction, cataclastic SECBs form most commonly, but CSBs are also present, particularly in the vicinity of reverse-faults.
3. All deformation bands form dominantly through cataclasis with pore collapse and grain size reduction
920 and result in an absolute porosity reduction of ca. 10% (from ~ 20% to 10%).
4. Normal faults and thrust faults show regular spacing of ca. 9 m over 10 km.
5. Most outcrops subject to quantitative spacing studies show mixed distributions of Pearson coefficients for the correlation between band spacing and position, which are interpreted as a consequence of multiple generations of deformation bands with similar attributes.
925
6. Most macroscopic faults probably form through linkage of precursory deformation bands across the stratigraphy. During this process, bands with regular spacing may become overprinted by later wall-, tip-, and interaction damage zones.
7. From a fluid flow perspective, the poly-deformed turbidites of the Hikurangi accretionary wedge constitute a highly compartmentalised rock body. Most faults and deformation bands likely act as
930 significant barriers to fluid flow.

Author Contributions

CES designed the study, and KRL and CES obtained research funding. KEE, CES, and CRS conducted the fieldwork. KEE visualised and analysed field data and conducted all microstructural analyses. KEE prepared the first draft of the manuscript, and all authors contributed to subsequent revisions and interpretations of the data.

935 **Competing Interests**

The authors declare that they have no conflict of interest.

Acknowledgements

The authors gratefully acknowledge funding by the Australian Research Council through Discovery grant DP170104550, which also supports KEE with a doctoral stipend. Emily and Anders Crofoot of Castlepoint Station
940 and their team are thanked warmly for access to their land and their hospitality. Gabriel Davey provided invaluable assistance in the field and with digitisation. This work was enabled by the use of the Central Analytical Research Facility hosted by the Institute for Future Environments at QUT. In addition, we thank Gus Luthje and Donald McAuley for thin-section preparation.

References

945   Ackermann, R. V., Schlische, R. W., and Withjack, M. O.: The geometric and statistical evolution of normal fault systems: an experimental study of the effects of mechanical layer thickness on scaling laws, Journal of Structural Geology, 23, 1803-1819, 2001.

Allmendinger, R. W., Cardozo, N., and Fisher, D. M.: Structural geology algorithms: Vectors and tensors, Cambridge University Press, 2011.

950   Anderson, E. M.: The dynamics of faulting, 1951.

Antonellini, M. and Aydin, A.: Effect of Faulting on Fluid-Flow in Porous Sandstones - Petrophysical Properties, AAPG Bull.-Am. Assoc. Petr. Geol., 78, 355-377, 1994.

Antonellini, M. and Aydin, A.: Effect of faulting on fluid flow in porous sandstones: geometry and spatial distribution, AAPG bulletin, 79, 642-670, 1995.

955   Antonellini, M. A., Aydin, A., and Pollard, D. D.: Microstructure of deformation bands in porous sandstones at Arches National Park, Utah, Journal of structural geology, 16, 941-959, 1994.

Audet, P., Bostock, M. G., Christensen, N. I., and Peacock, S. M.: Seismic evidence for overpressured subducted oceanic crust and megathrust fault sealing, Nature, 457, 76-78, 2009.

Aydin, A.: Faulting in sandstone, Dept. of Geology, Stanford University, 1977.

960   Aydin, A.: Small faults formed as deformation bands in sandstone, Pure and Applied Geophysics, 116, 913-930, 1978.

Aydin, A., Borja, R. I., and Eichhubl, P.: Geological and mathematical framework for failure modes in granular rock, Journal of Structural Geology, 28, 83-98, 2006.

Aydin, A. and Johnson, A. M.: Analysis of faulting in porous sandstones, Journal of Structural Geology, 5, 19-31, 1983.

Aydin, A. and Johnson, A. M.: Development of faults as zones of deformation bands and as slip surfaces in sandstone, Pure

965   and applied Geophysics, 116, 931-942, 1978.

Bai, T. and Pollard, D. D.: Closely spaced fractures in layered rocks: initiation mechanism and propagation kinematics, Journal of Structural Geology, 22, 1409-1425, 2000a.

Bai, T. and Pollard, D. D.: Fracture spacing in layered rocks: a new explanation based on the stress transition, Journal of Structural Geology, 22, 43-57, 2000b.

970   Bailleul, J., Chanier, F., Ferrière, J., Robin, C., Nicol, A., Mahieux, G., Gorini, C., and Caron, V.: Neogene evolution of lower trench-slope basins and wedge development in the central Hikurangi subduction margin, New Zealand, Tectonophysics, 591, 152-174, 2013.

Bailleul, J., Robin, C., Chanier, F., Guillocheau, F., Field, B., and Ferriere, J.: Turbidite Systems in the Inner Forearc Domain of the Hikurangi Convergent Margin (New Zealand): New Constraints on the Development of Trench-Slope Basins, Journal

975   of Sedimentary Research, 77, 263-283, 2007.

Ballance, P. F., HAYWARD, B. W., and BROOK, F. J. J. N.: Subduction regression of volcanism in New Zealand, 313, 820-820, 1985.

Ballance, P. F. J. J. o. t. R. S. o. N. Z.: Late Cenozoic time-lines and calc-alkaline volcanic arcs in northern New Zealand—further discussion, 18, 347-358, 1988.

980   Ballas, G., Fossen, H., and Soliva, R.: Factors controlling permeability of cataclastic deformation bands and faults in porous sandstone reservoirs, Journal of Structural Geology, 76, 1-21, 2015.

Ballas, G., Soliva, R., Benedicto, A., and Sizun, J.-P.: Control of tectonic setting and large-scale faults on the basin-scale distribution of deformation bands in porous sandstone (Provence, France), Mar. Pet. Geol., 55, 142-159, 2014.

Ballas, G., Soliva, R., Sizun, J. P., Fossen, H., Benedicto, A., and Skurtveit, E.: Shear-enhanced compaction bands formed at

985   shallow burial conditions; implications for fluid flow (Provence, France), Journal of Structural Geology, 47, 3-15, 2013.

Balsamo, F., Storti, F., Salvini, F., Silva, A., and Lima, C.: Structural and petrophysical evolution of extensional fault zones in low-porosity, poorly lithified sandstones of the Barreiras Formation, NE Brazil, Journal of Structural Geology, 32, 1806-1826, 2010.

Bésuelle, P.: Compacting and dilating shear bands in porous rock: Theoretical and experimental conditions, Journal of

990   Geophysical Research: Solid Earth, 106, 13435-13442, 2001.

Cai, J.: A super-critical stress model for polymodal faulting of rocks, Journal of Geodynamics, 130, 12-21, 2019.

Chanier, F. and Ferrière, J.: From a passive to an active margin: tectonic and sedimentary processes linked to the birth of an accretionary prism (Hikurangi margin, New Zealand), Bulletin, 162, 649-660, 1991.

Chanier, F., Ferrière, J., and Angelier, J.: Extensional deformation across an active margin, relations with subsidence, uplift,

995   and rotations: The Hikurangi subduction, New Zealand, Tectonics, 18, 862-876, 1999.

Chapple, W. M. and Spang, J. H. J. G. S. o. A. B.: Significance of layer-parallel slip during folding of layered sedimentary rocks, 85, 1523-1534, 1974.

Chemenda, A. I.: The formation of tabular compaction-band arrays: Theoretical and numerical analysis, Journal of the Mechanics and Physics of Solids, 57, 851-868, 2009.

1000   Chemenda, A. I., Ballas, G., and Soliva, R.: Impact of a multilayer structure on initiation and evolution of strain localization in porous rocks: Field observations and numerical modeling, Tectonophysics, 631, 29-36, 2014.

Chemenda, A. I., Wibberley, C., and Saillet, E.: Evolution of compactive shear deformation bands: Numerical models and geological data, Tectonophysics, 526-529, 56-66, 2012.

Delvaux, D. and Sperner, B.: Stress tensor inversion from fault kinematic indicators and focal mechanism data: the TENSOR

1005   program, Nieuwland, 2003. D.(ed.), New Insights into Structural Interpretation and Modelling, Geological Society, London, Special Publications 212, 75-100, 2003.

Donath, F. A. and Parker, R. B. J. G. S. o. A. B.: Folds and folding, 75, 45-62, 1964.

Eichhubl, P., Hooker, J. N., and Laubach, S. E.: Pure and shear-enhanced compaction bands in Aztec Sandstone, Journal of Structural Geology, 32, 1873-1886, 2010.

1010   Faulkner, D. R., Mitchell, T. M., Jensen, E., and Cembrano, J.: Scaling of fault damage zones with displacement and the implications for fault growth processes, Journal of Geophysical Research, 116, 2011.

Field, B., Pollock, R., and Browne, G.: Outcrop analog study of turbidites of the Miocene Whakataki Formation, New Zealand: Significance for reservoir volumetrics and modeling, 2006, 729.

Field, B. D.: Cyclicity in turbidites of the Miocene Whakataki Formation, Castlepoint, North Island, and implications for
1015   hydrocarbon reservoir modelling, New Zealand Journal of Geology and Geophysics, 48, 135-146, 2005.

Fossen, H. and Bale, A.: Deformation bands and their influence on fluid flow, AAPG bulletin, 91, 1685-1700, 2007.

Fossen, H., Schultz, R. A., Shipton, Z. K., and Mair, K.: Deformation bands in sandstone: a review, Journal of the Geological Society, 164, 755-769, 2007.

Fossen, H., Schultz, R. A., and Torabi, A.: Conditions and implications for compaction band formation in the Navajo
1020   Sandstone, Utah, Journal of Structural Geology, 33, 1477-1490, 2011.

Fossen, H., Soliva, R., Ballas, G., Trzaskos, B., Cavalcante, C., and Schultz, R. A.: A review of deformation bands in reservoir sandstones: geometries, mechanisms and distribution, Geological Society, London, Special Publications, 459, 9-33, 2018.

Fossen, H., Zuluaga, L. F., Ballas, G., Soliva, R., and Rotevatn, A.: Contractional deformation of porous sandstone: Insights from the Aztec Sandstone, SE Nevada, USA, Journal of Structural Geology, 74, 172-184, 2015.

1025   Fulljames, J., Zijerveld, L., Franssen, R., Møller-Pedersen, P., and Koestler, A.: Fault seal processes: systematic analysis of fault seals over geological and production time scales, Norwegian Petroleum Society Special Publications, 7, 51-59, 1997.

GNS: https://www.gns.cri.nz/Home/Our-Science/Land-and-Marine-Geoscience/Regional-Geology/Geological-Maps/1-250-000-Geological-Map-of-New-Zealand-QMAP, 2020.

Gross, M. R.: The origin and spacing of cross joints: examples from the Monterey Formation, Santa Barbara Coastline,
1030   California, Journal of Structural Geology, 15, 737-751, 1993.

Grujic, D. and Mancktelow, N. S. J. J. o. S. G.: Folds with axes parallel to the extension direction: an experimental study, 17, 279-291, 1995.

Healy, D., Blenkinsop, T. G., Timms, N. E., Meredith, P. G., Mitchell, T. M., and Cooke, M. L.: Polymodal faulting: time for a new angle on shear failure, Journal of Structural Geology, 80, 57-71, 2015.

1035   Healy, D. and Jupp, P.: Bimodal or quadrimodal? Statistical tests for the shape of fault patterns, Solid Earth, 9, 1051-1060, 2018.

Hu, Y. and Wang, K.: Bending-like behavior of thin wedge-shaped elastic fault blocks, Journal of Geophysical Research: Solid Earth, 111, 2006.

Jones, R. R., Holdsworth, R. E., McCaffrey, K. J., Clegg, P., and Tavarnelli, E.: Scale dependence, strain compatibility and
1040   heterogeneity of three-dimensional deformation during mountain building: a discussion, Journal of Structural Geology, 27, 1190-1204, 2005.

Karig, D. and Lundberg, N.: Deformation bands from the toe of the Nankai accretionary prism, Journal of Geophysical Research: Solid Earth, 95, 9099-9109, 1990.

Karner, S. L., Chester, J. S., Chester, F. M., Kronenberg, A. K., and Hajash, A.: Laboratory deformation of granular quartz
1045   sand: Implications for the burial of clastic rocks, Aapg Bulletin, 89, 603-625, 2005.

Kim, Y. S., Peacock, D. C. P., and Sanderson, D. J.: Fault damage zones, Journal of Structural Geology, 26, 503-517, 2004.

Klimczak, C., Soliva, R., Schultz, R. A., and Chéry, J.: Sequential growth of deformation bands in a multilayer sequence, Journal of Geophysical Research: Solid Earth, 116, 2011.

Knott, S. D., Beach, A., Brockbank, P. J., Brown, J. L., McCallum, J. E., and Welbon, A. I.: Spatial and mechanical controls
1050   on normal fault populations, Journal of Structural Geology, 18, 359-372, 1996.

Labaume, P., Maltman, A., Bolton, A., Tessier, D., Ogawa, Y., and Takizawa, S.: Scaly fabrics in sheared clays from the décollement zone of the Barbados accretionary prism, 1997, 59-78.

Laubach, S. E., Lamarche, J., Gauthier, B. D., Dunne, W. M., and Sanderson, D. J.: Spatial arrangement of faults and opening-mode fractures, Journal of Structural Geology, 108, 2-15, 2018.

1055   Laubach, S. E., Olson, J. E., and Gross, M. R.: Mechanical and fracture stratigraphy, AAPG bulletin, 93, 1413-1426, 2009.

Lee, J. M., Begg, J., and Forsyth, P.: Geology of the Wairarapa area, Institute of Geological & Nuclear Sciences, 2002.

Liu, J. and Regenauer-Lieb, K. J. P. R. E.: Application of percolation theory to microtomography of structured media: Percolation threshold, critical exponents, and upscaling, 83, 016106, 2011.

Lubiniecki, D. C., White, S. R., King, R. C., Holford, S. P., Bunch, M. A., and Hill, S. M.: Structural evolution of carbonate-
1060   hosted cataclastic bands adjacent to a major neotectonic fault, Sellicks Beach, South Australia, Journal of Structural Geology, 126, 11-24, 2019.

Luyendyk, B. P. J. G.: Hypothesis for Cretaceous rifting of east Gondwana caused by subducted slab capture, 23, 373-376, 1995.

Maerten, L., Maerten, F., Lejri, M., and Gillespie, P.: Geomechanical paleostress inversion using fracture data, Journal of
1065   structural Geology, 89, 197-213, 2016.

Main, I. G., Kwon, O., Ngwenya, B. T., and Elphick, S. C.: Fault sealing during deformation-band growth in porous sandstone, Geology, 28, 1131-1134, 2000.

Mair, K., Main, I., and Elphick, S. J. J. o. S. G.: Sequential growth of deformation bands in the laboratory, 22, 25-42, 2000.

Maison, T., Potel, S., Malié, P., Mählmann, R. F., Chanier, F., Mahieux, G., and Bailleul, J. J. C. M.: Low-grade evolution of
1070   clay minerals and organic matter in fault zones of the Hikurangi prism (New Zealand), 53, 579-602, 2018.

Maltman, A. J.: Deformation structures from the toes of active accretionary prisms, Journal of the Geological Society, 155, 639-650, 1998.

Martel, S. J.: Mechanical controls on fault geometry, Journal of Structural Geology, 21, 585-596, 1999.

Mathworks, T.: Optimization Toolbox User's Guide. The MathWorks Natick, MA, 2011.

1075   McCoy-West, A. J., Bennett, V. C., Puchtel, I. S., and Walker, R. J. J. G.: Extreme persistence of cratonic lithosphere in the southwest Pacific: Paleoproterozoic Os isotopic signatures in Zealandia, 41, 231-234, 2013.

Morgans, H.: New Zealand Cenozoic timescale (version 11/96), Institute of Geological & Nuclear Sciences Ltd., 1997.

Mortimer, N., Campbell, H. J., Tulloch, A. J., King, P. R., Stagpoole, V. M., Wood, R. A., Rattenbury, M. S., Sutherland, R., Adams, C. J., and Collot, J. J. G. t.: Zealandia: Earth's hidden continent, 27, 27-35, 2017.

1080   Neef, G.: Cretaceous and Cenozoic geology east of the Tinui Fault Complex in northeastern Wairarapa, New Zealand, New Zealand Journal of Geology and Geophysics, 38, 375-394, 1995.

Neef, G.: Geology of the Akitio area (1:50 000 metric sheet U25BD, east), northeastern Wairarapa, New Zealand, New Zealand Journal of Geology and Geophysics, 35, 533-548, 1992a.

Neef, G.: Turbidite deposition in five Miocene, bathyal formations along an active plate margin, North Island, New Zealand: 1085   with notes on styles of deposition at the margins of east coast bathyal basins, 78, 111-136, 1992b.

New Zealand Petroleum & Minerals, M. o. B., Innovation and Employment: New Zealand Petroleum Basins, 2013. 2013.

Nicol, A. and Childs, C.: Cataclasis and silt smear on normal faults in weakly lithified turbidites, Journal of Structural Geology, doi: https://doi.org/10.1016/j.jsg.2018.06.017, 2018. 2018.

Nicol, A., Childs, C., Walsh, J. J., and Schafer, K. W.: A geometric model for the formation of deformation band clusters, 1090   Journal of Structural Geology, 55, 21-33, 2013.

Nicol, A., Mazengarb, C., Chanier, F., Rait, G., Uruski, C., and Wallace, L.: Tectonic evolution of the active Hikurangi subduction margin, New Zealand, since the Oligocene, Tectonics, 26, n/a-n/a, 2007.

Nicol, A., VanDissen, R., Vella, P., Alloway, B., and Melhuish, A.: Growth of contractional structures during the last 10 m.y. at the southern end of the emergent Hikurangi forearc basin, New Zealand, New Zealand Journal of Geology and Geophysics, 1095   45, 365-385, 2002.

Ogilvie, S., Orribo, J., and Glover, P.: The influence of deformation bands upon fluid flow using profile permeametry and positron emission tomography, Geophysical Research Letters, 28, 61-64, 2001.

Ogilvie, S. R. and Glover, P. W.: The petrophysical properties of deformation bands in relation to their microstructure, Earth and Planetary Science Letters, 193, 129-142, 2001.

1100   Okubo, C. H. and Schultz, R. A.: Evolution of damage zone geometry and intensity in porous sandstone: insight gained from strain energy density, Journal of the Geological Society, 162, 939-949, 2005.

Olsson, W. and Holcomb, D.: Compaction localization in porous rock, Geophysical Research Letters, 27, 3537-3540, 2000.

Peacock, D. C. P., Dimmen, V., Rotevatn, A., and Sanderson, D. J.: A broader classification of damage zones, Journal of Structural Geology, 102, 179-192, 2017.

1105   Pollard, D. D. and Aydin, A.: Progress in understanding jointing over the past century, Geological Society of America Bulletin, 100, 1181-1204, 1988.

Qu, D., Tveranger, J., and Fachri, M.: Influence of deformation-band fault damage zone on reservoir performance, Interpretation, 5, SP41-SP56, 2017.

Rait, G., Chanier, F., and Waters, D. W. J. G.: Landward-and seaward-directed thrusting accompanying the onset of subduction 1110   beneath New Zealand, 19, 230-233, 1991.

Regenauer-Lieb, K., Veveakis, M., Poulet, T., Wellmann, F., Karrech, A., Liu, J., Hauser, J., Schrank, C., Gaede, O., and Fusseis, F.: Multiscale coupling and multiphysics approaches in earth sciences: Applications, Journal of Coupled Systems and Multiscale Dynamics, 1, 281-323, 2013a.

Regenauer-Lieb, K., Veveakis, M., Poulet, T., Wellmann, F., Karrech, A., Liu, J., Hauser, J., Schrank, C., Gaede, O., and 1115   Trefry, M.: Multiscale coupling and multiphysics approaches in earth sciences: Theory, Journal of Coupled Systems and Multiscale Dynamics, 1, 49-73, 2013b.

Rudnicki, J. W.: Compaction bands in porous rock, Bifurcations and Instabilities in Geomechanics, 2003. 29-39, 2003.

Rudnicki, J. W.: Shear and compaction band formation on an elliptic yield cap, Journal of Geophysical Research: Solid Earth, 109, 2004.

1120   Saillet, E. and Wibberley, C. A.: Evolution of cataclastic faulting in high-porosity sandstone, Bassin du Sud-Est, Provence, France, Journal of Structural Geology, 32, 1590-1608, 2010.

Schindelin, J., Arganda-Carreras, I., Frise, E., Kaynig, V., Longair, M., Pietzsch, T., Preibisch, S., Rueden, C., Saalfeld, S., and Schmid, B. J. N. m.: Fiji: an open-source platform for biological-image analysis, 9, 676, 2012.

Schueller, S., Braathen, A., Fossen, H., and Tveranger, J.: Spatial distribution of deformation bands in damage zones of 1125   extensional faults in porous sandstones: Statistical analysis of field data, Journal of Structural Geology, 52, 148-162, 2013.

Schultz, R. A.: Geologic Fracture Mechanics, Cambridge University Press, 2019.

Schultz, R. A. and Siddharthan, R.: A general framework for the occurrence and faulting of deformation bands in porous granular rocks, Tectonophysics, 411, 1-18, 2005.

Shipton, Z. K. and Cowie, P. A.: A conceptual model for the origin of fault damage zone structures in high-porosity sandstone, 1130   Journal of Structural Geology, 25, 333-344, 2003.

Shipton, Z. K. and Cowie, P. A.: Damage zone and slip-surface evolution over μm to km scales in high-porosity Navajo sandstone, Utah, Journal of Structural Geology, 23, 1825-1844, 2001.

Soliva, R., Ballas, G., Fossen, H., and Philit, S.: Tectonic regime controls clustering of deformation bands in porous sandstone, Geology, 44, 423-426, 2016.

1135   Soliva, R. and Benedicto, A.: Geometry, scaling relations and spacing of vertically restricted normal faults, Journal of Structural Geology, 27, 317-325, 2005.

Soliva, R., Benedicto, A., and Maerten, L.: Spacing and linkage of confined normal faults: importance of mechanical thickness, Journal of Geophysical Research: Solid Earth, 111, 2006.

Soliva, R., Schultz, R. A., Ballas, G., Taboada, A., Wibberley, C., Saillet, E., and Benedicto, A.: A model of strain localization 1140   in porous sandstone as a function of tectonic setting, burial and material properties; new insight from Provence (southern France), Journal of Structural Geology, 49, 50-63, 2013.

Solum, J. G., Brandenburg, J., Naruk, S. J., Kostenko, O. V., Wilkins, S. J., and Schultz, R. A.: Characterization of deformation bands associated with normal and reverse stress states in the Navajo Sandstone, Utah, AAPG bulletin, 94, 1453-1475, 2010.

Spörli, K.: New Zealand and oblique-slip margins: tectonic development up to and during the Cainozoic, Sedimentation in
oblique-slip mobile zones, 1980. 147-170, 1980.

Sternlof, K. R., Karimi-Fard, M., Pollard, D. D., and Durlofsky, L. J.: Flow and transport effects of compaction bands in
sandstone at scales relevant to aquifer and reservoir management, Water Resour. Res., 42, 16, 2006.

Strogen, D. P., Seebeck, H., Nicol, A., and King, P. R. J. J. o. t. G. S.: Two-phase Cretaceous–Paleocene rifting in the Taranaki
Basin region, New Zealand; implications for Gondwana break-up, 174, 929-946, 2017.

Świerczewska, A. and Tokarski, A. K.: Deformation bands and the history of folding in the Magura nappe, Western Outer
Carpathians (Poland), Tectonophysics, 297, 73-90, 1998.

Torabi, A., Fossen, H., and Braathen, A.: Insight into petrophysical properties of deformed sandstone reservoirs, Aapg Bulletin,
97, 619-637, 2013.

Ujiie, K., Maltman, A. J., and Sánchez-Gómez, M.: Origin of deformation bands in argillaceous sediments at the toe of the
Nankai accretionary prism, southwest Japan, Journal of Structural Geology, 26, 221-231, 2004.

Underhill, J. R. and Woodcock, N. H.: Faulting mechanisms in high-porosity sandstones; new red sandstone, Arran, Scotland,
Geological Society, London, Special Publications, 29, 91-105, 1987.

Walcott, R. I.: Geodetic strain and the deformational history of the North Island of New Zealand during the late Cainozoic,
Phil. Trans. R. Soc. Lond. A, 321, 163-181, 1987.

Walcott, R. J. G. J. I.: The kinematics of the plate boundary zone through New Zealand: a comparison of short-and long-term
deformations, 79, 613-633, 1984.

Wang, K. and Bilek, S. L.: Invited review paper: Fault creep caused by subduction of rough seafloor relief, Tectonophysics,
610, 1-24, 2014.

Wang, K. and Hu, Y. J. J. o. G. R. S. E.: Accretionary prisms in subduction earthquake cycles: The theory of dynamic Coulomb
wedge, 111, 2006.

Wells, P. J. B. r.: Burial history of late Neogene sedimentary basins on part of the New Zealand convergent plate margin, 2,
145-160, 1989.

Wong, T.-f. and Baud, P.: The brittle-ductile transition in porous rock: A review, Journal of Structural Geology, 44, 25-53,
2012.

Wong, T.-f., David, C., and Zhu, W.: The transition from brittle faulting to cataclastic flow in porous sandstones: Mechanical
deformation, Journal of Geophysical Research: Solid Earth, 102, 3009-3025, 1997.

Wong, T.-f., Szeto, H., and Zhang, J.: Effect of loading path and porosity on the failure mode of porous rocks, Applied
Mechanics Reviews, 45, 281-293, 1992.

Wong, T. F. and Zhu, W.: Brittle faulting and permeability evolution: Hydromechanical measurement, microstructural
observation, and network modeling, Faults and Subsurface Fluid Flow in the Shallow Crust, 1999. 83-99, 1999.

Wu, T.: Permeability prediction and drainage capillary pressure simulation in sandstone reservoirs, 2005. Texas A&M
University, 2005.

Xu, S. Q., Ben-Zion, Y., and Ampuero, J. P.: Properties of inelastic yielding zones generated by in-plane dynamic rupturesuI.
Model description and basic results, Geophysical Journal International, 191, 1325-1342, 2012.

Yielding, G., Freeman, B., and Needham, D. T.: Quantitative fault seal prediction, AAPG bulletin, 81, 897-917, 1997.

Zhang, J., Wong, T.-F., and Davis, D. M.: Micromechanics of pressure-induced grain crushing in porous rocks, Journal of
Geophysical Research, 95, 341, 1990.

Zuza, A. V., Yin, A., Lin, J., and Sun, M.: Spacing and strength of active continental strike-slip faults, Earth and Planetary
Science Letters, 457, 49-62, 2017.